

1 **Evolution of nasal and olfactory infection characteristics of SARS-CoV-2 variants**

2
3
4 Mengfei Chen¹, Andrew Pekosz^{2,3}, Jason S. Villano³, Wenjuan Shen¹, Ruifeng Zhou², Heather
5 Kulaga¹, Zhexuan Li¹, Sarah E. Beck³, Kenneth W. Witwer³, Joseph L. Mankowski³,
6 Murugappan Ramanathan Jr¹, Nicholas R. Rowan¹, and Andrew P. Lane¹

7
8 ¹Department of Otolaryngology-Head and Neck Surgery,

9 ²Department of Molecular Microbiology and Immunology, Bloomberg School of Public Health,
10 Baltimore, MD

11 ³Department of Molecular and Comparative Pathobiology, Johns Hopkins University School of
12 Medicine, Baltimore, MD

13
14 This work was funded by NIH Grants R01 AI132590, R01 DC016106 (A.P.L.), by the Johns
15 Hopkins Center of Excellence for Influenza Research and Surveillance, NIAID HHS
16 N2772201400007C (AP), and the generosity of the collective community of donors to the Johns
17 Hopkins University School of Medicine for COVID research.

18
19 Corresponding Author:
20 Andrew P. Lane, MD
21 Department of Otolaryngology – Head and Neck Surgery
22 Johns Hopkins Outpatient Center, 6th floor
23 601 N Caroline Street
24 Baltimore, MD 21287-0910
25 alane3@jhmi.edu

26
27 Co-corresponding Author:
28 Mengfei Chen, PhD
29 Department of Otolaryngology – Head and Neck Surgery
30 Johns Hopkins University School of Medicine
31 855 North Wolfe Street, Baltimore, MD 21205
32 mchen85@jhmi.edu

33
34

35

36

37 **Abstract**

38 SARS-CoV-2 infection of the upper airway and the subsequent immune response are early,
39 critical factors in COVID-19 pathogenesis. By studying infection of human biopsies in vitro and
40 in a hamster model in vivo, we demonstrated a transition in tropism from olfactory to respiratory
41 epithelium as the virus evolved. Analyzing each variants revealed that SARS-CoV-2 WA1 or
42 Delta infects a proportion of olfactory neurons in addition to the primary target sustentacular
43 cells. The Delta variant possesses broader cellular invasion capacity into the submucosa, while
44 Omicron displays longer retention in the sinonasal epithelium. The olfactory neuronal infection
45 by WA1 and the subsequent olfactory bulb transport via axon is more pronounced in younger
46 hosts. In addition, the observed viral clearance delay and phagocytic dysfunction in aged
47 olfactory mucosa is accompanied by a decline of phagocytosis related genes. Furthermore, robust
48 basal stem cell activation contributes to neuroepithelial regeneration and restores ACE2
49 expression post-infection. Together, our study characterized the nasal tropism of SARS-CoV-2
50 strains, immune clearance, and regeneration post infection. The shifting characteristics of viral
51 infection at the airway portal provides insight into the variability of COVID-19 clinical features
52 and may suggest differing strategies for early local intervention.

53

54 **Introduction**

55 Severe acute respiratory syndrome coronavirus 2 (SARS-CoV-2), the causative pathogen in
56 the worldwide pandemic of coronavirus disease 2019 (COVID-19), is readily transmitted via
57 respiratory droplets during close contact. The nasal cavity is the entry point of respiratory tract,
58 and the high viral load detected there indicates that this is the principal initial site of SARS-CoV-
59 2 infection and immune response^{1,2}. The loss of the sense of smell is common in patients infected

60 with the SARS-CoV-2 original WA1 and later Delta strains. Pathological studies visualizing
61 olfactory viral infection in postmortem samples of nasal respiratory and olfactory epithelium
62 partially explain the smell loss in COVID-19 patients³. Unlike the previous strains, Omicron
63 rarely causes olfactory loss, possibly suggesting a change in cellular tropism as the virus evolved.
64 Systematic characterization of the SARS-CoV-2 infection pattern in the nose is important for
65 understanding COVID-19 pathogenesis and for developing early local intervention.

66 The cellular tropism of SARS-Cov-2 in the nasal cavity is relevant to pathologic tissue damage
67 and to COVID testing. Cellular entry of SARS-CoV-2 depends on the binding of the virus spike
68 S protein to angiotensin-converting enzyme 2 (ACE2) in host tissue^{4,5}. The level of viral
69 receptors and its subcellular localization is a key determinant of susceptibility to infection. In
70 parallel with the gradually decreased ACE2 RNA expression pattern from the upper airway to
71 distal intrapulmonary regions^{6,7}, *in vitro* SARS-CoV-2 infection of human respiratory epithelial
72 cell cultures shows a gradient of diminishing infectivity (olfactory epithelial cells were not
73 included in these studies)⁷. Notably, we have observed up to 700-fold higher expression of ACE2
74 in the sustentacular cells of olfactory epithelium in comparison to respiratory epithelial cells in
75 human nose and trachea⁸. Whether the enrichment of ACE2 in the olfactory epithelium correlates
76 with more susceptibility to SARS-CoV-2 infection than respiratory cells, and how the infection
77 affects the olfactory sensory neurons are largely unknown.

78 Despite the substantially reduced COVID-19 incidence in adults after the rapid
79 vaccination program rollout, the unvaccinated population including young children, as well
80 as break-through infections by new variants, now comprise the majority cases. SARS-CoV-
81 2 infection typically causes mild acute airway illness in approximately 81% of COVID-19
82 patients; however, 14-17% of hospitalized cases experience severe symptoms and require

83 intensive care⁹. The severity of COVID-19 is highly age-related, with a fatality rate that can
84 reach 30.5% in patients of 85 years or older¹⁰, suggesting compromised anti-viral immunity with
85 aging. The correlation between aging and the cellular damage and subsequent immune response
86 to SARS-CoV-2 requires further investigation.

87 In this study, we perform *in vitro* infection of human nasal explants and show an extremely
88 high infection rate of SARS-CoV-2 WA1 strain in olfactory epithelium relative to the adjacent
89 respiratory epithelium. By comparing the infection patterns of WA1, Delta, and Omicron strains
90 in the hamster nasal cavity, we demonstrated a transition in tropism from olfactory to respiratory
91 epithelium as the virus evolved, providing insight into COVID-19 pathogenesis and diagnosis.
92 Using a WA1 strain infected hamster model, our additional findings demonstrate an age-
93 associated infection of olfactory neurons and impaired macrophage phagocytosis. These
94 findings indicate that the nasal viral replication and local immune defense could be a
95 potential target of early intervention.

96

97 **Results**

98 **WA1 strain primarily targets human olfactory neuroepithelium**

99 The human olfactory mucosa is located in the superior part of the nasal cavity contains
100 sustentacular cells and olfactory sensory neurons that is responsible for the sense of smell. To
101 examine the precise cellular tropism of SARS-CoV-2 in the nasal cavity including both
102 respiratory and olfactory epithelium, we initially performed WA1 strain *in vitro* infection
103 experiments using human nasal tissue discarded in endonasal sinus and skull base surgery in
104 COVID-19-negative individuals. To establish a reliable protocol to detect SARS-CoV-2 antigen,
105 we screened and verified 4 different antibodies for visualizing spike (S) or nucleocapsid protein

106 (NP) in the infected tissue sections (Extended Data Fig. 1a). The staining pattern of antibodies
107 predominant located in apical sustentacular cells is consistent with the viral RNA detected by
108 RNAscope analysis (Extended Data Fig. 1b).

109 Because the olfactory mucosa is irregularly distributed and surrounded by respiratory
110 epithelium in the human nasal cavity¹¹, we included the neuronal marker Tuj1 for the
111 verification of olfactory epithelium. By immunostaining with SARS-CoV-2 NP, we observed
112 substantial viral antigen in the Tuj1⁺ olfactory region at 9 hours post infection, but very little NP
113 in the adjacent Tuj1 negative respiratory epithelium (Fig. 1a,b). The vast majority of NP⁺ cells
114 co-localized with Krt18⁺ olfactory sustentacular cells (Extended Data Fig. 1c,d). Viral infection
115 caused extensive sustentacular cell death, with rapid detachment and sloughing into the nasal
116 lumen (Fig. 1a,b, and Extended Data Fig. 1c,d). Compared to the mock control (Extended Data
117 Fig. 1e), structural damage was readily detected in the olfactory mucosa but not in the respiratory
118 epithelium (Fig. 1a, b). A high viral infection ratio was also found in human olfactory cleft
119 specimens obtained from skull base surgery (Fig. 1c). Low viral infection was observed in 24
120 explants that only contained respiratory epithelium (Fig. 1d,e). We quantified the number of NP⁺
121 cells in 7 tissue explants, revealing 100-300-fold more infected cells in olfactory epithelium
122 compared to adjacent respiratory epithelium (Fig. 1e). These results together our earlier observed
123 enrichment of ACE2 expression illustrated an olfactory specific tropism of SARS-CoV-2 WA1
124 strain and explained the common symptom of anosmia in COVID-19 patients.

125 **Omicron variant shows transition in tropism from olfactory to respiratory epithelium**

126 As SARS-CoV-2 evolved, new variants including Delta and Omicron caused surges in
127 cases worldwide. The tropism of these different strains in the nasal cavity has not been
128 clarified. We next characterized the cellular tropism of WA1, Delta, and Omicron in nasal

129 mucosa using a hamster model. These experiments allowed us to determine whether the
130 observed cellular tropism of WA1 in human olfactory epithelium is applicable to new
131 variants in animal models and relates to subsequent disease pathogenesis.

132 The olfactory mucosa in the hamster nasal cavity is located in the posterior and dorsal
133 aspect, while the anterior and ventral areas are respiratory. We confirmed that the
134 expression of the neuronal marker Tuj1 in olfactory epithelium was mutually exclusive
135 with the respiratory marker Foxj1 in the nasal cavity (Extended Data Fig. 2a). Therefore,
136 the olfactory epithelium can be identified based on Tuj1 positive staining, the presence of
137 axon bundles, and the relatively increased thickness of the neuroepithelium. After SARS-
138 CoV-2 inoculation (1×10^5 TCID₅₀), we captured confocal images of the entire nasal cavity
139 in coronal sections at three different levels (Fig. 2a). At 4 days post infection (dpi), we verified
140 the extremely high viral antigen NP in the Tuj1⁺ olfactory epithelium of WA1 or Delta-infected
141 hamsters, with a sharp decline in the adjacent respiratory epithelium (Fig. 2b). About 79.2% or
142 70.3% length of Tuj1⁺ olfactory epithelium was infected by WA1 or Delta, respectively (Fig. 2b,
143 c). We observed that the expression of ACE2 in some OMP⁺ olfactory areas is low or
144 undetectable, interpreting the uninfected areas in WA1 or Delta treated groups (Extended Data
145 Fig. 2b).

146 In contrast to WA1 or Delta strain, the infected olfactory epithelium in Omicron group was
147 dramatically reduced to 6.7%, which is consistent with earlier reports of a comparatively lower
148 pathogenicity in lung of Omicron infected hamsters^{12,13}. The low infection rate of Omicron in
149 olfactory epithelium (Fig. 2b, c) seems to correlate with the low incidence of smell loss in
150 patients. Interestingly, we observed the Omicron infected NP⁺ nasal and sinus respiratory cells
151 was increased 7-10-fold when compared to WA1 or Delta, suggesting an olfactory to respiratory

152 tropism transition with the Omicron variant (Fig. 2b, d). These tropism patterns were further
153 demonstrated in sections of the anterior or posterior nasal cavity where the proportion of
154 respiratory epithelium is much greater or less, respectively (Extended Data Fig. 2c, 3a). Together,
155 these results identify that the SARS-Cov-2 variants have different tropism in nasal mucosa that
156 may play a role in the shifting pathogenic features of COVID-19 as the virus evolved.

157 To support the olfactory epithelial tropism of WA1 and Delta, we further performed qPCR
158 analysis of ACE2 expression in the entire nasal respiratory or olfactory mucosa in C57BL/6J
159 wildtype mouse at the ages of 2 weeks, 2 months, and 19 months. Compared to the nasal
160 respiratory epithelium, ACE2 mRNA transcription in adult olfactory epithelium was increased 5-
161 7-fold in 2m or 19m old animals (Fig. 2e). It should be noted that ACE2 mRNA levels in whole
162 olfactory mucosa are greatly diluted by the larger proportion of ACE2-low-to-negative cells
163 (neurons), relative to respiratory mucosa. In addition, ACE2 protein in human^{14,15} or mouse¹⁶
164 epithelial tissue is predominantly expressed at the apical surface. The more diffuse cellular
165 pattern of ACE2 staining in human autopsy specimens may result from post-mortem degradation.
166 In any putative human olfactory tissue sample, a neuronal marker must be utilized for
167 verification because the olfactory mucosa is irregularly distributed and surrounded by respiratory
168 epithelium. Consistent with previous data, we observed a gradually increased ACE2 expression
169 in olfactory mucosa from 2 weeks through adulthood^{17,18}. The level of ACE2 expression in nasal
170 respiratory mucosa was comparable between young and old animals (Fig. 2e). Together, the
171 ACE2 expression pattern supports the olfactory epithelium as a site of SARS-CoV-2 replication
172 especially for WA1 or Delta variants. The decreased olfactory tropism in the Omicron variant is
173 consistent with the recently reported endocytic entry pathway^{19,20}.

174 **Delta variant demonstrates greater infection of cells in the nasal submucosa**

175 In the lamina propria, we frequently detected NP⁺ cells in Delta inoculated hamsters at 4dpi.
176 Co-staining of NP and Pan-cytokeratin revealed that some of those infected cells were Bowman's
177 glands (Fig. 3a), the producer of specialized mucus critical for odor perception²¹. These results
178 are in line with our previously reported ACE2 expression in human biopsies⁸ and the observation
179 that SARS-CoV-2 targets Bowman's glands in postmortem samples by other groups³. The
180 number of NP⁺ Bowman's glands in Delta infected hamsters increased 21-fold when compared to
181 WA1, and is sharply decreased in Omicron group (Fig. 2b, 3b). Additionally, NP⁺ elongated
182 submucosal cells can be readily detected in olfactory and respiratory mucosa of Delta-infected
183 animals (Fig. 3c) but is dramatically reduced in Omicron treated hamsters. These NP⁺ cells are
184 aSMA⁺ but negative for Iba1 (macrophage marker) and Vimentin (mesenchymal and olfactory
185 ensheathing cell marker), suggesting the contractile myofibroblasts/mesenchymal cell lineage
186 (Fig. 3c, Extended Data Fig. 3b). The broader cell types targeted in the submucosa by the Delta
187 variant may increase the severity of tissue damage.

188 We next asked whether the infected submucosal cells are rapidly cleared or instead serve as an
189 ongoing viral reservoir. At 7dpi, we observed almost all the NP⁺ olfactory epithelial cells had
190 been lost, other than those in sloughed off debris in the nasal lumen. In the submucosa, except
191 NP⁺ axon in WA1 group, NP⁺ cell was barely detectable in animals infected with any of the 3
192 strains (Fig. 3d). These results in agreement with the reported viral titer analysis at 7dpi^{12,13}.
193 However, in the paranasal sinuses, an area was not examined in earlier studies^{12,13}, we detected a
194 small number of NP⁺ respiratory epithelial cells in WA1 but rarely in Delta treated hamsters at
195 7dpi. In parallel with the tropism transition from olfactory to respiratory epithelium, more
196 pronounced NP⁺ sinonasal epithelial cells (3.3 positive cells/mm epithelium) were observed in
197 Omicron variant-treated hamsters (Fig. 3d, e), suggesting a longer duration of the Omicron

198 variant infection in sinus epithelium relative to the ancestral SARS-CoV-2 strains. It is unknown
199 whether those Omicron -infected cells in the sinuses are actively transmitting virus at 7dpi.

200 **Age associated SARS-CoV-2 WA1 infection of olfactory sensory neurons**

201 While neurological symptoms, including headache, encephalitis, and altered mental status
202 have been reported in COVID-19 patients^{22,23}, the evidence of SARS-CoV-2 olfactory neuronal
203 infection is controversial^{3,24}. Earlier studies have shown SARS-CoV-2 RNA or viral antigen in
204 postmortem brain tissue samples^{25,26}, and rare infection observed in olfactory neurons in autopsy
205 tissue hints towards transmucosal invasion²⁷. The reported data have indicated SARS-CoV-2
206 infection affects neurons in the hamster model^{28,29}; however, Tuj1⁺ immature neurons are
207 normally located next to the basal layer, and the long foot-like processes of infected
208 sustentacular cells surrounding olfactory neurons could be mis-interpreted in earlier reports.
209 The direct evidence of olfactory neuronal infection and the factors that affect the frequency of
210 infection and entry to the brain remain to be clarified^{3,24}.

211 Given the high tropism of SARS-CoV-2 WA1 or Delta in olfactory mucosa, we took
212 advantage of a hamster model to examine WA1 or Delta infection in the olfactory neuronal
213 population. The hamster model allowed us to avoid the significant limitations of autopsy tissue,
214 including an often prolonged and severe disease course and tissue degradation during the
215 postmortem interval. We utilized a higher viral inoculum (1×10^7 TCID₅₀) to generate more
216 uniform infections that would allow us to identify variation across age groups³⁰. As expected, we
217 observed the vast majority of NP⁺ cells were apical sustentacular cells³¹ in WA1 infected
218 hamsters (Extended Data Fig. 1a,b) at 4 dpi. Interestingly, in the superior turbinate of posterior
219 nasal cavity, we observed NP labeling of a small portion of cells located in the olfactory sensory
220 neuronal layer and their axon bundles (Fig. 4a). Co-staining of NP with neuronal markers

221 Tuj1 (immature) and OMP (mature) revealed viral infection in a subset of cells from the neuronal
222 lineage (Fig. 4b, c). NP⁺/OMP⁺ infected olfactory neurons were also detected in Delta variant
223 treated hamsters (Extended Data Fig. 4a). We detected viral antigen travel along the Tuj1⁺ axon
224 from epithelium to the lamina propria (Fig. 4d, e). In axon bundles, NP co-localized with Tuj1⁺
225 or OMP⁺ axons (Extended Data Fig. 4b, c) but did not colocalize with Vimentin⁺ ensheathing
226 cells (Extended Data Fig. 4d). In addition, we confirmed the olfactory neuronal infection by
227 WA1 or Delta at 1×10^5 TCID50 (Extended Data Fig. 4e, f). Precise quantification of the number
228 of infected olfactory neurons is a challenge because the intensity of marker staining in infected
229 and dying cells subsides³ compared to normal cells (Extended Data Fig. 4g) and because the
230 epithelium sloughs off in some areas. We observed at least 20 NP⁺/OMP⁺ or Tuj1⁺ neurons in
231 each section of hamster infected with the WA1 at 1×10^5 TCID50. Compared to WA1, olfactory
232 neuronal infection is sharply decreased in Delta and rare in Omicron group. These data suggested
233 that WA1 or Delta can also infect a proportion of olfactory sensory neurons, in addition to
234 sustentacular cells that are the primary target in the upper airway. We therefore used WA1 strain
235 for the following aging-related experiments.

236 The rare expression of ACE2 in olfactory sensory neurons^{8,16} suggests that neuronal entry may
237 mediated by other receptors such as Neuropilin-1 (Nrp1)^{32,33}. In the olfactory epithelium, Nrp1
238 was expressed in the olfactory nerve in the embryonic stage and in immature neurons after
239 birth^{34,35}. By using qPCR analysis, we detected 2.7-fold reduction of Nrp1 mRNA in the
240 olfactory epithelium of 19-month-old compared to 2 weeks young mice (Extended Data Fig. 5a).
241 Age related Nrp1 reduction in the olfactory epithelium was also verified by
242 immunohistochemistry. About 34.2% of Tuj1⁺ olfactory neurons express Nrp1 in young mice but
243 only 9.7% of Tuj1⁺ neurons in the aged group display a low level of Nrp1 (Extended Data Fig.

244 5b-d). A few mature olfactory neurons in young mice also express Nrp1 (Extended Data Fig. 5b).
245 In addition, Nrp1 can be detected in the axon bundles and periglomerular cells in young olfactory
246 bulb, but are sharply declined in aged mice (Extended Data Fig. 5b,e).

247 The age-related pattern of Nrp1 expression indicated a potential higher efficiency of SARS-
248 CoV-2 infection in olfactory neurons in young population. To assess whether age could be a
249 factor mediating neuronal infection in the olfactory epithelium, we performed SARS-CoV-2
250 WA1 (1×10^7 TCID₅₀) infection experiments using young (1-month) and aged (8-month)
251 hamsters. At 6 dpi, viral antigen (NP) could be readily detected in the axon bundles in young
252 hamsters, but infected axons were dramatically decreased in older hamsters (Fig. 4 f-h). We also
253 examined the WA1-infected human explants and identified a remarkable increase of viral load in
254 Tuj1⁺ neurons and axon bundles in tissue from young individuals (<30 years old) (Fig. 4i, j). As
255 expected, we observed 38.9% of Tuj1⁺ olfactory neurons co-express Nrp1 in younger human
256 biopsies, but the proportion of Tuj1⁺/Nrp1⁺ neurons dramatically reduced (7.2%) in older adults
257 (Fig. 4k, l). Together, these results support age-dependent olfactory neuron infection and axonal
258 transport.

259 **Increased olfactory bulb axonal transport of WA1 in young hamsters**

260 The increased frequency of viral NP in the axons of younger animals indicated that SARS-
261 CoV-2 WA1 may be prone to accessing the brain in this population. To verify this hypothesis,
262 we examined the olfactory bulbs of 1 and 8-month old hamsters. At 6 dpi, we detected NP⁺
263 axons located in the olfactory nerve layer (ONL) in young hamsters (Fig. 5a,b), suggesting the
264 viral transport to olfactory bulb. Compared to the young hamsters, infected axons are rarely
265 detected in the older group (Fig. 5a-c). Co-staining analysis of serial sections verified that the NP
266 signal is located in the Tuj1⁺ olfactory nerve layer (Fig. 5d). In the leptomeningeal layer where

267 the viral RNA signal was detected in postmortem samples³, the NP antibody staining was not
268 detectable in hamster (Fig. 5a-d). In addition, the observed leptomeningeal viral RNA staining
269 was speculated to be extracellular virions instead of intracellular viral RNA synthesized by
270 infected cells³. In parallel to the greater olfactory bulb viral transport, the number of Iba1⁺
271 microglia cells in young olfactory bulb was increased 1.7-fold compared with older group (Fig.
272 5e). No viral antigen could be detected in the mock control.

273 Immunostaining of horizontal sections crossing the olfactory mucosa and forebrain region
274 revealed a massive number of NP⁺ axons traveling from the lateral olfactory epithelium to
275 olfactory bulb in young, but not aged, hamsters at 6 dpi (Extended Data Fig. 6a-f). In line with
276 the reported Nrp1 expression in lateral olfactory nerve, which contains axons from turbinate
277 neurons³⁶, the infected axon in the septum nerve was rare. NP⁺ axons could also be detected in
278 glomeruli where the olfactory sensory neuron axon terminal projections synapse with OB mitral
279 cells (Fig. 5b, d) at 6dpi. As a consequence of olfactory viral transport, we observed Caspase-3⁺
280 apoptotic cells and virus RNA in the glomerular layer at 4dpi (Fig. 5f, and Extended Data Fig.
281 6g,h) in the young group. These Caspase-3⁺ cells were negative for Iba1 or the neuronal marker
282 NeuN. The transported virus in olfactory bulb appears to lose the capacity for replication based
283 on the restriction of NP signal to axons in the outer olfactory nerve layer and glomeruli at 6dpi
284 (Fig. 5b-d). Despite the close anatomic relationship between the olfactory mucosa and the nearby
285 OB axons, no obvious transmucosal viral antigen NP was displayed except within axons.

286 Similar to ACE2 expression in lung vascular endothelial cells³⁷, ACE2 in the mouse or
287 hamster olfactory bulb is mainly located in the blood vessels (Extended Data Fig. 6i,j). We
288 observed CD45⁺/Iba1⁻ immune cells infiltrating into the olfactory bulb in SARS-Cov2 infected
289 hACE2 mice (Extended Data Fig. 6k,l), indicating passage of leukocytes across an impaired

290 blood-brain barrier. Given the lack of lymphatic vessels in brain parenchyma, it is unlikely that
291 viral infection of the olfactory bulb occurs via this route³⁸. The inflammatory response in the
292 hamster brain is not as severe as in the hACE2 mouse model, therefore the vascular damage is
293 also likely much milder in hamster. Together, these results support that SARS-CoV-2 WA1 can
294 gain access to the olfactory bulb region in the brain mainly through olfactory neuronal axons
295 with higher frequency in younger population, while virus replication is limited.

296 **Age-related viral clearance delay and phagocytic dysfunction in the olfactory mucosa**

297 The tropism of SARS-CoV-2 in olfactory epithelium indicates the capacity of local immune
298 system against viral infection could involve in the pathogenesis of COVID-19. It has been
299 reported that reduced innate antiviral defenses including type I and type III interferons coupled
300 with a hyperinflammatory response is the major cause of disease severity and death in COVID-
301 19 patients^{39,40}. Corresponding to the high viral load in olfactory epithelium, our qPCR analysis
302 revealed an extensive upregulation of the anti-viral gene *Ifng* (type II interferon) in the nasal
303 turbinate tissue post infection (Extended Data Fig. 7a), suggesting activated local immune
304 defense. We next studied the potential age-related alternation of olfactory immune response to
305 SARS-CoV-2 infection.

306 Because of the limited cross-reactivity of CD45 antibodies with hamster tissue, we took
307 advantage of the mouse adapted SARS-CoV-2 (maSARS) infection model in C57BL/6J
308 wildtype mice⁴¹. Normally, a low number of CD45⁺ immune cells and Iba1⁺
309 macrophages/dendritic cells reside in the mouse olfactory mucosa. In maSARS infected group,
310 we observed striking CD45⁺ immune cell infiltration into the lamina propria, crossing the basal
311 cell layer and migrating into the neuroepithelium, suggesting a nasal immune defense in response
312 to viral infection (Fig. 6a). On 6 dpi, approximately 48.3% of CD45⁺ immune cells in olfactory

313 mucosa were Iba1⁺ macrophages/dendritic cells, which is similar to single-cell RNA sequencing
314 data of BALF samples from critical COVID 19 patients^{42,43}.

315 In hamsters, intranasal inoculation of SARS-CoV-2 induced massive shedding of NP⁺ infected
316 cells into the nasal lumen at 4 dpi (Fig. 6b-d), consistent with our findings in infected human
317 olfactory biopsies. Iba1⁺ macrophages/dendritic cells were widely distributed in the olfactory
318 mucosa and the detached cells in the lumen (Fig. 6b,c). Co-staining analysis showed that the
319 Iba1⁺ macrophages are the major population producing CXCL10 (Extended Data Fig. 7b), a
320 chemokine that has been reported in macrophages from COVID-19 patients' BALF sample.
321 Notably, 72% of Iba1⁺ cells were also positive for viral NP antigen at 4dpi (Fig. 6b), indicating
322 uptake of infected cell debris. In addition, some of the apoptotic cells sloughed into the nasal
323 lumen were Iba1⁺/Caspase-3⁺, suggesting the viral clearance by macrophages (Fig. 6c).

324 Compared to the young hamsters, the number of Iba1⁺ cells in the nasal lumen significantly
325 increased in the older group at 6dpi (Fig. 6d,e). In parallel to the increased macrophages, we
326 observed the number of remaining NP⁺ cells/debris in the serial sections of older hamster nasal
327 cavities was increased 3.7-fold when compared to young hamsters (Fig. 6d,f), in line with the
328 reported prolonged virus load/delayed viral clearance in older COVID patients⁴⁴. The delayed
329 viral clearance could be a consequence of impaired phagocytic function in aging macrophages,
330 as reported in an influenza infection model⁴⁵.

331 By analyzing a previously published single cell RNA sequencing (scRNA-seq) dataset⁴⁶
332 derived from mouse lung CD45⁺ inflammatory cells, we noted significant reduction of
333 phagocytosis related genes⁴⁷ including Clec4n (Dectin2), Fabp5, Fpr2, and Cd9 in old
334 macrophage/dendritic lineages compared to young mice (Fig. 6g). We further verified that the
335 expression of Dectin2 was dominantly located in Iba1⁺ macrophages/dendritic cells in olfactory

336 mucosa of young mice and dramatically declined with age (Fig. 6h). Collectively, our data
337 support that the macrophages are the critical population involved in SARS-CoV-2 defense, and
338 their impaired viral clearance capacity could involve in the prolonged virus retention in the
339 olfactory mucosa of the aged population.

340 **Regenerated olfactory epithelium regains ACE2 expression**

341 Given the robust reparative capacity of the olfactory mucosa⁴⁸ and the rapid reconstitution
342 post SARS-CoV2 infection^{31,49}, we next systematically examined post-viral stem cell-mediated
343 regeneration using an adult hamster model (2-month old). As a consequence of viral infection,
344 nearly complete loss of neuroepithelium was observed at 4dpi, and ACE2 was not detectable in
345 newly regenerated epithelium (Fig. 7a). Compared to the single layer of Krt5-expressing
346 olfactory stem cells in mock control, SARS-CoV-2 induced widespread epithelial damage and
347 activated robust basal cell proliferation simultaneously (Extended Data Fig. 7c). qPCR analysis
348 revealed that the increased expression of Sox2 (basal cell /sustentacular cell marker), Lgr5
349 (globose basal cell marker), and Tubb3 (immature neuron marker) was coincident with gradual
350 re-expression of ACE2 as olfactory epithelium regeneration proceeded (Fig. 7b, Extended Data
351 Fig. 7d). The expression of ACE2 and the olfactory sensory neuron marker, OMP, recovered to
352 78% and 56% of mock on 28 dpi, respectively (Fig. 7b,c). The incomplete recovery of OMP on
353 28 dpi partially may explain the slow return of olfactory function in human cases with severe
354 damage.

355 Coincident with epithelial repair, production of CXCL10 in Iba1+ macrophages vanished in
356 both the young and old groups on 6dpi (Extended Data Fig. 7b). Compared to the old group, the
357 newly regenerated olfactory epithelium in young hamsters is significantly thicker at 6dpi (Fig.
358 7d,e), suggesting age-related delay in regeneration post infection. Furthermore, recovery of

359 ACE2 protein could be detected in hamsters at 28 dpi, and ACE2 expression was also observed
360 in a COVID-19 patient who had lost the sense of smell (Fig. 7f,g).

361 **Discussion**

362 Understanding the cellular tropism and properties of SARS-CoV-2 infection of the upper
363 airway could provide valuable insights for predicting the pathogenicity of new variants.
364 Consistent with the enrichment of ACE2 in human olfactory sustentacular cells⁸, we herein
365 present greatly enhanced infection efficiency in human and hamster olfactory epithelium,
366 suggesting that this site is potentially critical for initial SARS-CoV-2 infection and replication,
367 especially for the WA1 and Delta strains. The tropism transition from olfactory to respiratory
368 observed in the Omicron variant may explain the low prevalence of anosmia, while the extended
369 duration that Omicron resides in the sinonasal respiratory epithelium may contribute to increased
370 transmission. Our observations, together with the clinical findings of high viral loads in the nasal
371 passages of COVID-19 patients^{1,2}, suggests that the nasal cavity is an important site of SARS-
372 CoV-2 infection, cell damage, and host immune reaction in nasal cavity.

373 The mechanisms underlying olfactory loss in SARS-CoV-2 infection are difficult to
374 disentangle from a number of pathological processes at multiple anatomic levels²⁴.
375 Quantification of SARS-CoV-2 in nasal and throat swabs reveals a gradual decrease in viral load
376 soon after symptom onset^{2,50}, suggesting a short pathological process in the nose. Together with
377 these findings, the rapid detachment of infected olfactory epithelium presented here may explain
378 variation in viral loads detected on nasal swabs². The subsequent neuroepithelial structural
379 damage upon viral targeting of supporting sustentacular cells and olfactory neurons plausibly
380 underlies the high incidence of olfactory dysfunction in COVID-19 patients. Importantly, the
381 detached olfactory epithelium likely carries a large amount of virus, and shedding of these

382 infected cells has the potential for aerosolization, exacerbating lung infection, and facilitating
383 transmission between individuals. Other factors include the disrupted nuclear architecture,
384 downregulated olfactory receptor expression⁵¹ in mild infection, as well as the infection of
385 Bowman's glands³ may also account for the olfactory dysfunction. However, the contribution of
386 the small proportion of olfactory neurons that are become infected based on our observations is
387 likely very limited.

388 Whether and how SARS-CoV-2 gains access to the brain has been investigated intensively and
389 debated widely²⁴. Unlike the obvious infection of the brain in hACE2-expressing mice after
390 SARS-CoV-2 inoculation⁵²⁻⁵⁴, viral antigen in hamster brain was not detectable^{28,55,56} while one
391 study recovered SARS-CoV-2 from brain tissue⁵⁵. A recent study in a hamster model showed
392 limited viral antigen located in nasal OMP⁺ olfactory axons²⁹. The presence of SARS-CoV-2
393 RNA or viral antigen in human postmortem brain tissue reveals that the virus may access the
394 brain even though neuronal infection is rare²⁵⁻²⁷. To avoid the tissue autolysis associated with
395 long postmortem intervals, a bedside endoscopic tissue harvest procedure was developed by
396 Khan et al³. In 85 postmortem samples analyzed from COVID-19 cases, even though a uniform
397 sustentacular cell infection was visualized in the olfactory mucosa of a patient within 4 days of
398 diagnosis, no infection in olfactory sensory neurons was identified. It should be noted that the
399 samples in the study by Khan et al were limited to relatively aged (>62 years) patients. Although
400 most children and adolescents are spared from severe COVID-19, it is reported that 22%
401 experience neurologic involvement and 12% develop life-threatening neurologic sequelae⁵⁷.
402 Abnormal neuroimaging manifestations, including acute disseminated encephalomyelitis-like
403 changes, were also reported in children with COVID-19⁵⁸. Based on infection of young and old
404 hamsters, our observations provide strong evidence that SARS-CoV-2 WA1 targets a subset of

405 mature and immature olfactory neurons, and gains access to the brain through axon transport in
406 an age-dependent manner. The higher proportion of Nrp1⁺ olfactory neuron in the young
407 population may be associated with the increased neuronal infection. It should be noted that a role
408 for other SARS-CoV-2 entry molecules besides Nrp1⁵⁹ for the invasion process cannot be
409 excluded from our data.

410 The unique targeting of SARS-CoV-2 (WA1 and Delta strains) to a small neuronal population
411 may have impeded discovery to date. As previously mentioned, the absence of evidence for
412 olfactory sensory neuron infection in postmortem samples could be attributed to the older age of
413 the cohort studied³. The enhanced olfactory bulb viral transport and subsequent greater level of
414 microglial infiltration in younger hosts may call for a reassessment of neurological impairment in
415 children. Indeed, recent clinical evidence indicates a recurring pattern of disease with SARS-
416 CoV2-related abnormal CNS neuroimaging in infected children without pre-existing conditions⁵⁸.
417 Therefore, the long-term consequences of brain infection require further investigation.

418 In line with previous observations of aging-related deficits of macrophage phagocytosis in
419 influenza infection models⁴⁵, the delayed SARS-CoV-2 clearance in older hamsters' olfactory
420 mucosa and in COVID-19 patients may represent a compromised phagocytic function of aged
421 macrophages. The prolonged viral retention may correlate with disease severity in aged COVID-
422 19 patients or with increased risk of transmission. Therefore, the local immune defense in nasal
423 olfactory and respiratory mucosa represents a potential target for early intervention and
424 prevention.

425 Robust olfactory basal cell activation efficiently regenerates sustentacular cells and restores
426 ACE2 expression. The continued ACE2 expression in the olfactory epithelium may be important,
427 given that anti-SARS-CoV-2 antibodies decay after approximately 6 months from the onset of

428 symptoms, especially in individuals with mild COVID-19 disease⁶⁰. The rapid restoration of
429 ACE2 expression in olfactory epithelium may provide an avenue for re-infection in recovered
430 COVID-19 patients. Taken together, our study identifies the tropism of SARS-CoV-2 WA1 and
431 Delta in olfactory epithelium and the transport of virus to the brain through olfactory neuron
432 axons, especially in younger hosts. In addition, the longer duration of Omicron infection in
433 sinonasal epithelium raises the possibility that early topical intranasal treatment may accelerate
434 viral clearance and reduce transmission.

435 It should be noted that the observed viral tropism in this study only represents characteristics
436 of infection in the nasal cavity. While our observations demonstrate a high olfactory tropism of
437 WA1 and Delta, the infection is not limited to the olfactory epithelium, and recent RNAseq⁶¹ and
438 RNAscope or immunohistochemistry³ evidence using COVID-19 patient samples suggests the
439 presence of nasal respiratory epithelial infection as well. The extent to which nasal viral load
440 affects lower respiratory infection is not known. In addition, the relatively low amount of virus
441 transported into the olfactory bulb reported here unlikely causes significant neurologic change
442 other than microglial activation and inflammation. Even though the specific cellular tropism in
443 the nasal cavity for each SARS-CoV-2 strain was identified here, it remains to be determined
444 which group of mutations in Spike S protein is associated with altered tropism. Given the
445 predominance of respiratory epithelium by area in the human nasal cavity, the enhanced
446 respiratory infection and the extended viral retention in sinus epithelium may contribute to the
447 increased transmissibility of Omicron, and calls for a reassessment of early local intervention.

448

449

450 **References**

- 451 1. Wang, W., *et al.* Detection of SARS-CoV-2 in Different Types of Clinical Specimens. *Jama* (2020).
- 452 2. Zou, L., *et al.* SARS-CoV-2 Viral Load in Upper Respiratory Specimens of Infected Patients. *N Engl J Med* **382**, 1177-1179 (2020).
- 453
- 454 3. Khan, M., Yoo, S.-J., Clijsters, M., Backaert, W. & Vanstapel, A. Visualizing in deceased COVID-19
455 patients how SARS-CoV-2 attacks the respiratory and olfactory mucosae but spares the olfactory
456 bulb. *Cell In Press*(2021).
- 457 4. Zhou, P., *et al.* A pneumonia outbreak associated with a new coronavirus of probable bat origin.
458 *Nature* **579**, 270-273 (2020).
- 459 5. Hoffmann, M., *et al.* SARS-CoV-2 Cell Entry Depends on ACE2 and TMPRSS2 and Is Blocked by a
460 Clinically Proven Protease Inhibitor. *Cell* **181**, 271-280 (2020).
- 461 6. Sungnak, W., *et al.* SARS-CoV-2 entry factors are highly expressed in nasal epithelial cells
462 together with innate immune genes. *Nat Med* (2020).
- 463 7. Hou, Y.J., *et al.* SARS-CoV-2 Reverse Genetics Reveals a Variable Infection Gradient in the
464 Respiratory Tract. *Cell* **182**, 429-446 e414 (2020).
- 465 8. Chen, M., *et al.* Elevated ACE-2 expression in the olfactory neuroepithelium: implications for
466 anosmia and upper respiratory SARS-CoV-2 entry and replication. *The European respiratory*
467 *journal* **56**(2020).
- 468 9. Wu, Z. & McGoogan, J.M. Characteristics of and Important Lessons From the Coronavirus
469 Disease 2019 (COVID-19) Outbreak in China: Summary of a Report of 72314 Cases From the
470 Chinese Center for Disease Control and Prevention. *Jama* (2020).
- 471 10. Wiersinga, W.J., Rhodes, A., Cheng, A.C., Peacock, S.J. & Prescott, H.C. Pathophysiology,
472 Transmission, Diagnosis, and Treatment of Coronavirus Disease 2019 (COVID-19): A Review.
473 *Jama* **324**, 782-793 (2020).
- 474 11. Child, K.M., Herrick, D.B., Schwob, J.E., Holbrook, E.H. & Jang, W. The Neuroregenerative
475 Capacity of Olfactory Stem Cells Is Not Limitless: Implications for Aging. *J Neurosci* **38**, 6806-6824
476 (2018).
- 477 12. Halfmann, P.J., *et al.* SARS-CoV-2 Omicron virus causes attenuated disease in mice and hamsters.
478 *Nature* (2022).
- 479 13. Suzuki, R., *et al.* Attenuated fusogenicity and pathogenicity of SARS-CoV-2 Omicron variant.
480 *Nature* (2022).
- 481 14. Hamming, I., *et al.* Tissue distribution of ACE2 protein, the functional receptor for SARS
482 coronavirus. A first step in understanding SARS pathogenesis. *J Pathol* **203**, 631-637 (2004).
- 483 15. Lee, I.T., *et al.* ACE2 localizes to the respiratory cilia and is not increased by ACE inhibitors or
484 ARBs. *Nature communications* **11**, 5453 (2020).
- 485 16. Brann, D.H., *et al.* Non-neuronal expression of SARS-CoV-2 entry genes in the olfactory system
486 suggests mechanisms underlying COVID-19-associated anosmia. *Sci Adv* **6**(2020).
- 487 17. Bunyavanich, S., Do, A. & Vicencio, A. Nasal Gene Expression of Angiotensin-Converting Enzyme
488 2 in Children and Adults. *Jama* **323**, 2427-2429 (2020).
- 489 18. Bilinska, K., Jakubowska, P., Von Bartheld, C.S. & Butowt, R. Expression of the SARS-CoV-2 Entry
490 Proteins, ACE2 and TMPRSS2, in Cells of the Olfactory Epithelium: Identification of Cell Types
491 and Trends with Age. *ACS chemical neuroscience* **11**, 1555-1562 (2020).
- 492 19. Zhao, H., *et al.* SARS-CoV-2 Omicron variant shows less efficient replication and fusion activity
493 when compared with Delta variant in TMPRSS2-expressed cells. *Emerging microbes & infections*
494 **11**, 277-283 (2022).
- 495 20. Hui, K.P.Y., *et al.* SARS-CoV-2 Omicron variant replication in human bronchus and lung ex vivo.
496 *Nature* (2022).
- 497 21. Lee, K.H., Wells, R.G. & Reed, R.R. Isolation of an olfactory cDNA: similarity to retinol-binding
498 protein suggests a role in olfaction. *Science* **235**, 1053-1056 (1987).

- 499 22. Mao, L., *et al.* Neurologic Manifestations of Hospitalized Patients With Coronavirus Disease 2019
500 in Wuhan, China. *JAMA Neurol* (2020).
- 501 23. Varatharaj, A., *et al.* Neurological and neuropsychiatric complications of COVID-19 in 153
502 patients: a UK-wide surveillance study. *Lancet Psychiatry* **7**, 875-882 (2020).
- 503 24. Xydakis, M.S., *et al.* Post-viral effects of COVID-19 in the olfactory system and their implications.
504 *The Lancet. Neurology* **20**, 753-761 (2021).
- 505 25. Matschke, J., *et al.* Neuropathology of patients with COVID-19 in Germany: a post-mortem case
506 series. *The Lancet. Neurology* **19**, 919-929 (2020).
- 507 26. Solomon, I.H., *et al.* Neuropathological Features of Covid-19. *N Engl J Med* **383**, 989-992 (2020).
- 508 27. Meinhardt, J., *et al.* Olfactory transmucosal SARS-CoV-2 invasion as a port of central nervous
509 system entry in individuals with COVID-19. *Nat Neurosci* (2020).
- 510 28. Zhang, A.J., *et al.* SARS-CoV-2 infects and damages the mature and immature olfactory sensory
511 neurons of hamsters. *Clin Infect Dis* (2020).
- 512 29. de Melo, G.D., *et al.* COVID-19-related anosmia is associated with viral persistence and
513 inflammation in human olfactory epithelium and brain infection in hamsters. *Science*
514 *translational medicine* (2021).
- 515 30. Jiang, L., *et al.* A bacterial extracellular vesicle-based intranasal vaccine against SARS-CoV-2
516 protects against disease and elicits neutralizing antibodies to wild-type and Delta variants.
517 *Journal of extracellular vesicles* **11**, e12192 (2022).
- 518 31. Bryche, B., *et al.* Massive transient damage of the olfactory epithelium associated with infection
519 of sustentacular cells by SARS-CoV-2 in golden Syrian hamsters. *Brain Behav Immun* **89**, 579-586
520 (2020).
- 521 32. Cantuti-Castelvetri, L., *et al.* Neuropilin-1 facilitates SARS-CoV-2 cell entry and infectivity. *Science*
522 **370**, 856-860 (2020).
- 523 33. Daly, J.L., *et al.* Neuropilin-1 is a host factor for SARS-CoV-2 infection. *Science* **370**, 861-865
524 (2020).
- 525 34. Miller, A.M., Maurer, L.R., Zou, D.J., Firestein, S. & Greer, C.A. Axon fasciculation in the
526 developing olfactory nerve. *Neural Dev* **5**, 20 (2010).
- 527 35. Pasterkamp, R.J., De Winter, F., Holtmaat, A.J. & Verhaagen, J. Evidence for a role of the
528 chemorepellent semaphorin III and its receptor neuropilin-1 in the regeneration of primary
529 olfactory axons. *J Neurosci* **18**, 9962-9976 (1998).
- 530 36. Schwarting, G.A., *et al.* Semaphorin 3A is required for guidance of olfactory axons in mice. *J*
531 *Neurosci* **20**, 7691-7697 (2000).
- 532 37. Alon, R., *et al.* Leukocyte trafficking to the lungs and beyond: lessons from influenza for COVID-
533 19. *Nat Rev Immunol* (2020).
- 534 38. Louveau, A., *et al.* CNS lymphatic drainage and neuroinflammation are regulated by meningeal
535 lymphatic vasculature. *Nat Neurosci* **21**, 1380-1391 (2018).
- 536 39. Merad, M. & Martin, J.C. Pathological inflammation in patients with COVID-19: a key role for
537 monocytes and macrophages. *Nat Rev Immunol* **20**, 355-362 (2020).
- 538 40. Blanco-Melo, D., *et al.* Imbalanced Host Response to SARS-CoV-2 Drives Development of COVID-
539 19. *Cell* **181**, 1036-1045 e1039 (2020).
- 540 41. Rathnasinghe, R., *et al.* The N501Y mutation in SARS-CoV-2 spike leads to morbidity in obese and
541 aged mice and is neutralized by convalescent and post-vaccination human sera. *medRxiv* (2021).
- 542 42. Liao, M., *et al.* Single-cell landscape of bronchoalveolar immune cells in patients with COVID-19.
543 *Nat Med* **26**, 842-844 (2020).
- 544 43. Chua, R.L., *et al.* COVID-19 severity correlates with airway epithelium-immune cell interactions
545 identified by single-cell analysis. *Nat Biotechnol* **38**, 970-979 (2020).

- 546 44. Zheng, S., *et al.* Viral load dynamics and disease severity in patients infected with SARS-CoV-2 in
547 Zhejiang province, China, January-March 2020: retrospective cohort study. *Bmj* **369**, m1443
548 (2020).
- 549 45. Wong, C.K., *et al.* Aging Impairs Alveolar Macrophage Phagocytosis and Increases Influenza-
550 Induced Mortality in Mice. *Journal of immunology* **199**, 1060-1068 (2017).
- 551 46. Mogilenko, D.A., *et al.* Comprehensive Profiling of an Aging Immune System Reveals Clonal
552 GZMK(+) CD8(+) T Cells as Conserved Hallmark of Inflammaging. *Immunity* **54**, 99-115 e112
553 (2021).
- 554 47. Jaitin, D.A., *et al.* Lipid-Associated Macrophages Control Metabolic Homeostasis in a Trem2-
555 Dependent Manner. *Cell* **178**, 686-698 e614 (2019).
- 556 48. Schwob, J.E., *et al.* Stem and progenitor cells of the mammalian olfactory epithelium: Taking
557 poietic license. *J Comp Neurol* **525**, 1034-1054 (2017).
- 558 49. Urata, S., *et al.* Regeneration Profiles of Olfactory Epithelium after SARS-CoV-2 Infection in
559 Golden Syrian Hamsters. *ACS chemical neuroscience* **12**, 589-595 (2021).
- 560 50. Wolfel, R., *et al.* Virological assessment of hospitalized patients with COVID-2019. *Nature* (2020).
- 561 51. Zazhytska, M., *et al.* Non-cell-autonomous disruption of nuclear architecture as a potential
562 cause of COVID-19-induced anosmia. *Cell* **185**, 1052-1064 e1012 (2022).
- 563 52. Zheng, J., *et al.* COVID-19 treatments and pathogenesis including anosmia in K18-hACE2 mice.
564 *Nature* (2020).
- 565 53. Winkler, E.S., *et al.* SARS-CoV-2 infection of human ACE2-transgenic mice causes severe lung
566 inflammation and impaired function. *Nat Immunol* **21**, 1327-1335 (2020).
- 567 54. Golden, J.W., *et al.* Human angiotensin-converting enzyme 2 transgenic mice infected with
568 SARS-CoV-2 develop severe and fatal respiratory disease. *JCI Insight* **5**(2020).
- 569 55. Imai, M., *et al.* Syrian hamsters as a small animal model for SARS-CoV-2 infection and
570 countermeasure development. *Proc Natl Acad Sci U S A* **117**, 16587-16595 (2020).
- 571 56. Sia, S.F., *et al.* Pathogenesis and transmission of SARS-CoV-2 in golden hamsters. *Nature* **583**,
572 834-838 (2020).
- 573 57. LaRovere, K.L., *et al.* Neurologic Involvement in Children and Adolescents Hospitalized in the
574 United States for COVID-19 or Multisystem Inflammatory Syndrome. *JAMA Neurol* **78**, 536-547
575 (2021).
- 576 58. Lindan, C.E., *et al.* Neuroimaging manifestations in children with SARS-CoV-2 infection: a
577 multinational, multicentre collaborative study. *Lancet Child Adolesc Health* **5**, 167-177 (2021).
- 578 59. Peng, R., Wu, L.A., Wang, Q., Qi, J. & Gao, G.F. Cell entry by SARS-CoV-2. *Trends in biochemical*
579 *sciences* **46**, 848-860 (2021).
- 580 60. Ibarrondo, F.J., *et al.* Rapid Decay of Anti-SARS-CoV-2 Antibodies in Persons with Mild Covid-19.
581 *N Engl J Med* **383**, 1085-1087 (2020).
- 582 61. Ziegler, C.G.K., *et al.* Impaired local intrinsic immunity to SARS-CoV-2 infection in severe COVID-
583 19. *Cell* **184**, 4713-4733 e4722 (2021).
- 584 62. Chen, M., Reed, R.R. & Lane, A.P. Chronic Inflammation Directs an Olfactory Stem Cell Functional
585 Switch from Neuroregeneration to Immune Defense. *Cell Stem Cell* **25**, 501-513 e505 (2019).
- 586 63. Leopold, D.A., *et al.* Anterior distribution of human olfactory epithelium. *The Laryngoscope* **110**,
587 417-421 (2000).

588

589

590 **Figure Legends**

591 **Fig. 1. SARS-Cov-2 WA1 selectively targets human olfactory neuroepithelium**

592 **a,b**, Confocal images of SARS-CoV-2 viral antigen NP (red, Novus, NB100-56576) and
593 olfactory neuronal marker β -III Tubulin (Tuj1, green) in superior turbinate biopsies from 2
594 separate patients. Images were obtained under tile scan mode, which covered olfactory and
595 adjacent respiratory epithelium in the same piece of tissue. Boxed area in **(b)** was highlighted in

596 **Extended Data Fig. 1c, d.**

597 **c**, Co-staining of NP and Tuj1 in human biopsy collected from the olfactory cleft.

598 **d**, Representative image of NP overlapped with Tuj1-negative ciliated cell (brightfield).

599 Confocal image was obtained from a biopsy which contains only respiratory epithelium.

600 **e**, Quantification of NP⁺ cells per mm tissue. 24 independent specimens have exclusively

601 respiratory epithelium (RE), while 7 specimens contained both respiratory and olfactory

602 epithelium (OE).

603 Arrowheads **(a-c)** indicate the detachment of infected cells. Data in **(e)** are represented as mean \pm

604 S.D. *p* value was calculated by one-way ANOVA. Scale bars, 50 μ m **(a and b)**; 20 μ m **(c,d)**.

605

606 **Fig. 2. Omicron variant shows tropism transition from olfactory to respiratory epithelium**

607 **a**, Scheme of the tissue section. To avoid variability across different animals, frozen sections

608 were collected and examined at three consistent levels (L1–3) representing the anterior (mainly

609 respiratory epithelium), middle (respiratory + Olfactory epithelium), and posterior (mainly

610 olfactory epithelium).

611 **b**, Confocal images of NP and Tuj1-labeled hamster nasal sections at L2. WA1, Delta, and

612 Omicron infected hamsters were examined on 4 dpi. Boxed areas are highlighted at bottom.

613 Scale bars = 500 μ m.

614 **c**, Percentage of the infected olfactory epithelium. The total length of Tuj1⁺ or NP⁺/Tuj1⁺
615 epithelium in each section at L1-3 were quantified using Image J.
616 **d**, Quantification of NP⁺ cells in nasal respiratory epithelium. The total NP⁺ cells in Tuj1⁻
617 respiratory epithelium including paranasal sinuses of each section were counted.
618 **e**, qPCR analysis of ACE2 expression in mouse nasal respiratory or olfactory epithelium at age
619 of 2 weeks, 2months, and 19months. The entire nasal respiratory or olfactory epithelium from
620 the same animal were isolated separately.
621 Data are represented as mean \pm S.D. Statistical significance was determined by unpaired two-
622 tailed *t*-test. Each data point represents an individual animal.

623

624 **Fig. 3. Delta variant infects cells in submucosa of the nose**

625 **a**, Representative image shows NP⁺/Pan-Keratin⁺ Bowman's glands in Delta treated hamsters.
626 **b**, Quantification of infected Bowman's glands. The average number of NP⁺ Bowman's glands
627 in one 14 μ m section was calculated. 3 sections per animal were counted.
628 **c**, Confocal image shows NP⁺/ α -SMA⁺ myofibroblasts. Hamsters infected with Delta variant on
629 4dpi were examined.
630 **d**, Co-staining of Tuj1 and NP in nasal sections at 7dpi. Whole nasal cavity images were
631 captured using a tile scan and z stack mode on a 14 μ m section. Boxed area in Omicron infected
632 hamster is highlighted on the right. Scale bars = 500 μ m.
633 **e**, Quantification of NP⁺ respiratory epithelial cells in paranasal sinuses. 3 sections per animal
634 was counted.
635 Data are represented as mean \pm S.D. Statistical significance was determined by unpaired two-
636 tailed *t*-test. Each data point represents an individual animal.

637

638 **Fig. 4. Age associated SARS-Cov-2 infection in olfactory sensory neurons**

639 **a-c**, Confocal image showing WA1-infected hamster olfactory epithelium at 4dpi. Insert in **(a)**

640 highlighting an NP stained axon bundle (horizontal section). Arrowheads indicate virus infected

641 Tuj1⁺ immature **(b)** or OMP⁺ mature **(c)** sensory neurons (coronal sections). White line indicated

642 the basal layer of epithelium.

643 **d, e**, NP⁺ axon travel from neuroepithelium to lamina propria and merge into Tuj1⁺ axon bundle.

644 **f-h**, Quantification of NP⁺ axons in young and old hamsters at 6dpi. Representative images show

645 horizontal **(f)** or coronal sections **(g)**. NP⁺ axons were quantified per μm of the diameter of axon

646 bundle.

647 **i,j**, Representative images showing NP located in Tuj1⁺ human olfactory neurons **(j)** and the

648 percentage of NP⁺ cells in Tuj1⁺ population **(i)**. Dotted line in **(j)** indicates virus infected NP⁺

649 axon. Arrowheads denote NP⁺/Tuj1⁺ neurons compared to uninfected cells (empty arrowhead).

650 Infected biopsies from 3 young donors (age 25-33 years) and 5 biopsies from older donors (age

651 54-72 years) were quantified for Tuj1⁺ neuronal infection.

652 **k,l**, Representative images of Nrp1 expression in human olfactory epithelium **(k)** and

653 quantification of Nrp1⁺ cells in Tuj1⁺ population **(l)**. 3 biopsies from young (age 20-30 years)

654 and 4 biopsies from older donors (age 68-79 years) were examined for Nrp1 expression. Images

655 in **(k)** were captured with 3 μm Z-stack and exported by maximum intensity projections. Each

656 data point represents an individual sample from hamster **(h)**, or human **(i and l)**. Details of

657 human biopsies can be found in Supplementary Table 1. Data are represented as mean \pm S.D.

658 Statistical significance was determined by unpaired two-tailed t-test. Scale bars, 20 μm .

659

660 **Fig. 5. Increased olfactory bulb transport of SARS-CoV-2 in young hamsters**

661 **a-c**, Confocal images of Iba1 and NP co-staining in hamster olfactory bulbs. Arrowheads

662 indicate infected axon.

663 **d**, Co-staining of NP and Tuj1 in a serial section next to panel **(b)**.

664 **e**, Quantification of Iba1⁺ microglials in hamster olfactory bulb. Each data point in **(d)** represents

665 an individual hamster sample. Data are represented as mean \pm S.D. Statistical significance was

666 determined by unpaired two-tailed t-test.

667 **f**, Confocal image of cleaved caspase-3⁺/NeuN⁻ apoptotic cells (arrowheads) in the glomerular

668 layer at 4dpi.

669 Images were captured with 3 μ m **(a-d)** or 4 μ m **(f)** Z-stack and exported by maximum intensity

670 projections. Olfactory bulb tissues were collected from young and old hamsters on 6dpi **(a-d)** or

671 from mock control. Scale bars, 50 μ m, **(a-d)**; 20 μ m, **(f)**. ONL, olfactory nerve layer; GL,

672 glomerular layer; EPL, external plexiform layer; MCL, mitral cell layer. Boxed areas are

673 highlighted at bottom. Dotted circles indicate glomeruli.

674

675 **Fig. 6. Age-associated delay in viral clearance in olfactory mucosa**

676 **a**, Representative images showing CD45 and Iba1 co-staining in olfactory mucosa. Mock or

677 maSARS-Cov2 infected wildtype mice were examined at 6dpi.

678 **b**, Co-immunostaining shows Iba1⁺ macrophages engulfing NP⁺ debris in hamster olfactory

679 mucosa at 4dpi.

680 **c**, Representative image of Iba1 and cleaved caspase-3 co-staining in hamster at 4dpi.

681 Arrowheads highlight the Iba1⁺ macrophages undergoing apoptosis.

682 **d**, Representative images showing Iba1 or NP staining in serial sections. Each panel combines 6
683 40x images acquired under tile scan mode. Young or old hamsters' olfactory tissues were
684 examined at 6dpi.
685 **e,f**, Quantification of Iba1⁺ (**e**) or NP⁺ (**f**) cells in hamster nasal olfactory lumen at 6dpi. Serial
686 sections (**d**) from 4 different levels were quantified.
687 **g**, Violin plots showing the differentially expressed Clec4n (Dectin2) or Fpr2 in young and old
688 macrophage/dendritic lineage.
689 **h**, Confocal images of Iba1 and Dectin2 co-staining in mouse olfactory mucosa.
690 Each data point represents an individual hamster sample. Statistical significance was determined
691 by unpaired two-tailed t-test. The white dotted line in (**a-c**) indicates the basement membrane.
692 Scale bars, 20 μm (**a-c, h**); 50 μm (**d**).

693

694 **Fig. 7. Regeneration of olfactory epithelium and re-expression of ACE2**

695 **a**, Confocal images showing ACE2 (red) and Krt5⁺ horizontal basal cells (green) in olfactory
696 epithelium of mock or SARS-CoV-2 infected hamster at 4 dpi.

697 **b,c**, qPCR analysis of ACE2 (**b**) or OMP (**c**) mRNA expression in SARS-CoV-2 infected
698 hamster turbinate lysate at indicated time points.

699 **d,e**, Representative images of Krt5⁺ cells in newly regenerated olfactory epithelium (**d**) on 6dpi,
700 and quantification of epithelium thickness (**e**). The thickness of septal olfactory epithelium was
701 measured using Zen lite "line" function. For each section, 8 spots were measured randomly.

702 **f**, Confocal image showing regenerated hamster olfactory epithelium expression of ACE2 at
703 28dpi.

704 **g**, Representative image shows ACE2 and Tuj1⁺ olfactory neurons in an olfactory biopsy from a
705 COVID-19 patient on day 12 post diagnosis.

706 Dots in graph represent independent animal. Data are represented as mean \pm S.D. *p* value was
707 calculated by unpaired two-tailed Student's *t* test. Scale bars, 20 μ m.

708

709 **Extended Data Fig. 1 Detection of SARS-Cov-2 in the olfactory neuroepithelium.**

710 **a**, SARS-Cov-2 antibody testing. 1 anti-spike S and 3 different anti-NP were verified to be
711 reliable for frozen section immunohistochemistry. Hamster olfactory tissue was examined at 4dpi.
712 All 4 antibodies stained in the same pattern showing intensive viral load mainly located in the
713 apical sustentacular cell layer. No signal could be detected in mock control. Catalog number for
714 each antibody is presented accordingly.

715 **b**, RNAscope analysis showing SARS-Cov-2 viral RNA on 4dpi in hamster olfactory epithelium.

716 **c,d**, Co-staining of NP and sustentacular cell marker Krt18. Image was captured from the boxed
717 area in panel **(b)** of Figure 1.

718 **e**, Confocal image of NP and Tuj1 staining in mock control. Scale bars, 20 μ m.

719

720 **Extended Data Fig. 2 Decreased Omicron variant infection in hamster olfactory epithelium.**

721 **a**, Co-staining of neuronal marker Tuj1 and respiratory epithelium marker Foxj1 in mouse nasal
722 cavity. Scale bar, 200 μ m.

723 **b**, Representative image shows OMP and rabbit anti ACE2 co-staining in hamster turbinate
724 horizontal section. Intense ACE2 expression is seen in OMP⁺ olfactory epithelium. The green
725 arrows show the respiratory-olfactory transition area with lower ACE2 expression. Scale bar,
726 100 μ m.

727 **c**, Confocal images show the distribution of NP and Tuj1 in a coronal section at L1 of the nasal
728 cavity. Tissues were examined on 4dpi, boxed areas were highlighted at bottom. Note that NP
729 was dramatically declined from Tuj1 negative respiratory epithelium (RE) in hamsters infected
730 with WA1 or Delta. The respiratory infection in Omicron group was markedly increased. Scale
731 bars = 500 μ m.

732

733 **Extended Data Fig. 3 Tropism of SARS-CoV-2 variants in the posterior nasal mucosa.**

734 **a**, Confocal images showing the distribution of NP and Tuj1 in posterior nasal cavity sections at
735 4dpi. Coronal sections at L3 were examined, where the proportion of olfactory epithelium is
736 predominant. The olfactory epithelium infection in the Omicron group was decreased remarkably.
737 Scale bar = 500 μ m.

738 **b**, Co-staining of NP and Iba1 (macrophage marker) or NP and Vimentin (mesenchymal cell and
739 olfactory ensheathing cell marker) in Delta infected hamster. Scale bars = 20 μ m.

740 The white dotted line in **(b)** indicates the basement membrane.

741

742 **Extended Data Fig. 4 SARS-Cov-2 WA1 and Delta variants infect olfactory sensory**
743 **neurons.**

744 **a**, Co-staining of NP and OMP in olfactory epithelium. 5 weeks-old hamsters were infected with
745 SARS-CoV-2-Delta variant (1×10^7 TCID50) and were examined on 4dpi. Arrowhead indicates
746 an infected neuron.

747 **b,c**, Confocal images show co-localization of NP with Tuj1⁺ or OMP⁺ axon. **(b)** shows a larger
748 view of Figure 2f. Boxed areas in **(b)** were highlighted at bottom. 1m **(b)** or 7-8 weeks-old **(c)**
749 hamsters were infected with WA1.

750 **d**, Representative image shows NP signal does not colocalize with Vimentin in axon bundles.
751 **e,f**, Co-staining of NP and OMP in olfactory epithelium.
752 **g**, Confocal image shows Tuj1⁺ immature olfactory neurons in mock group.
753 7-8 week-old hamsters were infected WA1 (**d, e**) or Delta variant (**f**) at 1×10^5 TCID50 and were
754 examined at 4dpi. Scale bars, 20 μ m.

755

756 **Extended Data Fig. 5 Expression of Nrp1 in mouse olfactory epithelium and bulb**

757 **a**, qPCR analysis of Nrp1 expression in mouse olfactory mucosa at ages 2 weeks, 2 months, and
758 19 months. Each data point represents an individual mouse (n=3).

759 **b,c**, Immunostaining analysis shows the expression of Nrp1 in the Tuj1⁺ immature olfactory
760 neurons and axon bundles. Confocal images were acquired from horizontal section of young (1
761 month) and old (8 month) mice. Boxed areas were highlighted on right. In young mice, a few
762 mature neurons above the Tuj1⁺ cells also express a low level of Nrp1.

763 **d**, Percentage of Nrp1 expressing cells in Tuj1⁺ immature neurons. Olfactory tissues from
764 wildtype mice were examined at the indicated age groups.

765 **e**, Confocal images show the expression of Nrp1 in young and old mouse olfactory bulb. Data
766 are represented as mean \pm S.D. Statistical significance was determined by unpaired two-tailed *t*-
767 test. Arrowheads highlight Nrp1⁺ cells in glomerular layer. Scale bars, 20 μ m (**b,c**); 50 μ m (**e**).

768

769 **Extended Data Fig. 6 Increased brain transport of SARS-CoV-2 in young hamsters**

770 **a-f**, Confocal image capturing a cross section of olfactory epithelium and olfactory bulb. SARS-
771 CoV-2-infected young or old hamsters were examined at 6 dpi. Boxed areas highlight the
772 infected lateral olfactory axons crossing the cribriform plate and projecting to the olfactory bulb.

773 Images were captured with 4 μm Z-stack and exported by maximum intensity projections. OE,
774 olfactory epithelium; OB, olfactory bulb.
775 **g**, RNAscope analysis shows viral RNA in SARS-Cov-2 infected hamster OB glomeruli at 4dpi.
776 **h**, Co-staining of Caspase-3 and Iba1 in olfactory bulb at 4dpi.
777 **h,i**, Confocal image shows co-staining of endothelial cell marker CD31 and ACE2 in mouse (**h**)
778 or hamster (**i**, ACE2 only) olfactory bulb.
779 **j**, Immunostaining of CD45 and microglia marker Iba1 in the olfactory bulb of hACE2 mice at 6
780 dpi. Arrowheads indicate Iba1 negative immune cells. In the hACE2 strain, human ACE2
781 overexpression was driven by mouse Krt18 promoter. Scale bars, 100 μm (**a,d**); 50 μm (**h-j**).

782

783 **Extended Data Fig. 7 Regeneration of the olfactory epithelium**

784 **a**, qPCR analysis of *Ifng* expression in turbinate tissues. SARS-CoV-2 infected hamsters were
785 examined at indicated time points.
786 **b**, Dynamic of Iba1⁺ macrophages infiltration and CXCL10 expression in hamster olfactory
787 epithelium.
788 **c**, Representative images show Krt5⁺ basal cells expressing proliferation marker Ki67 on 4dpi in
789 hamster olfactory epithelium.
790 **d**, qPCR analysis of *Sox2*, *Lgr5*, and *Tubb3* expression in turbinate samples at indicated time
791 points.
792 Data are represented as mean \pm S.D. Statistical significance was determined by unpaired two-
793 tailed *t*-test. Each data point represents an individual mouse. Scale bars, 20 μm .

794

795

796

797

798

799

800

801

802

803

804

805

806

807

808

809

810

811 **Methods**

812 **Human nasal explant *in vitro* infection.** The research protocol involving human specimens was
813 approved by the Johns Hopkins institutional review board, and all subjects provided signed
814 informed consent. Nasal biopsies included olfactory epithelial and/or respiratory epithelial
815 samples were collected from chronic rhinosinusitis (CRS) patients and control subjects
816 undergoing endonasal surgical approaches for non-CRS disease processes⁶². All patients were
817 tested negative for COVID-19 before surgery. In this study, the majority of biopsies were taken
818 from superior turbinates. The human olfactory mucosa is predominantly distributed on the dorsal

819 aspect of the nasal vault⁶³. The superomedial portion of superior turbinate that comprises part of
820 the olfactory cleft contains olfactory epithelium, while the inferior and lateral side is entirely
821 respiratory epithelium. Therefore, the coronal sections of superior turbinate samples in this study
822 include both olfactory and respiratory epithelium, with a much smaller proportion of olfactory
823 relative to respiratory. Notably, over 60% of the superior turbinate biopsies contained solely
824 respiratory epithelium. Other specimens were obtained from the olfactory cleft septal mucosa.
825 More details about the clinical specimens are listed in Supplementary Table 1.

826 Human biopsies were placed in PneumaCult medium (Stemcell Technologies) and sent for
827 infection immediately. SARS-CoV-2 infection experiments were conducted in a biosafety level 3
828 facility at the Bloomberg School of Public Health, Johns Hopkins University. After 2 hours
829 incubation with SARS-CoV-2/USA/WA1/2020 (BEI Resources) at 5×10^5 TCID₅₀ per mL, the
830 tissues were washed in PBS and transfer into fresh medium at 37°C. Mock controls were
831 maintained in medium without virus. Tissues were fixed at 9 hours post infection in 4% PFA at
832 4°C for 24 hours. 6 control (2 females and 4 males ranged from 45 to 63 years old) and 27 CRS
833 biopsies (11 females and 16 males ranged from 25 to 76 years old) were used for detailed
834 immunohistochemistry analysis.

835 Human biopsies for Nrp1 staining were collected from 3 young (20-30 years) and 4 older (68-
836 79years) subjects. Tissues were fixed in 4% PFA at 4°C overnight, and the olfactory
837 neuroepithelium identity was verified by Tuj1 staining.

838 **Animal *in vivo* infection**

839 Animal infection experiments were carried out in a biosafety level 3 facility at Johns Hopkins
840 Research Animal Resources (RAR) in compliance with the established ethical guidelines.
841 Animal experimental procedures were approved by the Animal Care and Use Committee at the

842 Johns Hopkins University. Animal infection experiments were conducted using wildtype
843 C57BL/6J mice, Syrian golden hamsters (HsdHan®: AURA, Envigo, Haslett MI), and hACE2
844 mice (B6.Cg-Tg(K18-ACE2)2PrImn/J, JAX, Bar Harbor, Maine). In hACE2 strain, the human
845 ACE2 was driven by the mouse Krt18 promoter. 1×10^7 TCID50/ml of SARS-CoV-
846 2/USA/WA1/2020 or 2.4×10^7 TCID50/ml of Delta variant (SARS-CoV-2/USA/MD-
847 HP05660/2021 B.1.617.2) in 100 μ L Dulbecco's modified Eagle medium (DMEM) was
848 intranasally inoculated to hamsters (50 μ l per nare). 6.3×10^5 PFU in 20 μ L (10 μ L per nare)
849 was administered intranasally to hACE2 mice. The mouse-adapted SARS-CoV-2 (courtesy of
850 Michael Schotsaert, Icahn School of Medicine at Mt. Sinai) infection⁴¹ was performed as 10 μ L
851 per nare, 2.5×10^8 PFU. Mock control animals received equivalent volume of DMEM alone.

852 **Tissue processing**

853 Animals were euthanized in biosafety level 3 facility at indicated time points. After anesthetized
854 with avertin and transcardially perfused with PBS followed by 4% PFA, the skull bone was
855 removed, and the head was postfixed in 4% PFA at 4°C for 3 days. After decalcification in
856 TBD2 solution (6764003, Thermo) overnight and washing in PBS, tissues were equilibrated
857 sequentially in 15% and 30% sucrose, then embedded in Optimum Cutting Temperature (OCT,
858 Tissue-Tek) for sectioning Fixed human biopsies were processed similarly and embedded in
859 OCT without TBD2 treatment. Frozen sections were processed at 12 μ m using MICROM
860 HM560 cryostat (Thermo).

861 **Immunohistochemistry**

862 The immunostaining process was carried out on cryosections after an antigen retrieval step.
863 Briefly, sections were washed in PBS and then blocked in 2% BSA containing 0.2% Triton X-
864 100 at 4 °C overnight, followed by incubation with primary antibodies at 4 °C overnight. The

865 following primary antibodies was used: Rabbit anti-SARS-CoV-2 Nucleoprotein (1:200, Novus,
866 NB100-56576), Rabbit anti- SARS-CoV-2 Nucleoprotein (1:500, GeneTex, GTX135357),
867 Rabbit anti- SARS-CoV Nucleoprotein (1:1000, Rockland, 200-401-A50), Rabbit anti- SARS-
868 CoV-2 Spike S (1:200, Sino Biological, 40150-R007), Goat anti-ACE2 (1:100, R&D, AF933, for
869 human samples), Rabbit anti-ACE2 (1:100, Thermo, MA5-32307, for hamster samples), Goat
870 anti-Neuropilin-1 (1:200, R&D, AF566) Mouse anti-Keratin 18 (1:500, Novus, NB500-306),
871 Goat anti OMP (1:500, Wako, 544-10001), Mouse anti- α SMA (1:100, R&D MAB1420);
872 Chicken anti-Vimentin (Novus NB300-223); Goat anti-Foxj1 (1:200, R&D AF3619); Mouse
873 anti-NeuN (1:1000, BioLegend, 834502); Rat anti-CD45 (1:300, Ebioscience, 14-0451-81), Rat
874 anti-CD31(1:50, BD, 550274), Rabbit anti-Krt5 (1:500, Covance, PRB-160P), Chicken anti-Krt5
875 (1:500, BioLegend, 905904), Mouse anti Tuj1 (1:300, BioLegend, 801203), Rabbit anti Iba1
876 (1:500, Wako, 019-19741), Rabbit anti-Cleaved Caspase-3 (1:300, Cell signaling, 9664), Rat anti
877 Dectin2 (1:200, Bio-Rad, MCA2415T), and Goat anti-CXCL10(1:100, R&D, AF-466-NA).

878 After washing in PBS three times, the tissue sections were incubated with Alexa Fluor
879 conjugated, highly cross-adsorbed, secondary antibodies along with DAPI for nuclear
880 counterstaining. The donkey-derived Alexa Fluor-conjugated secondary antibodies included anti-
881 mouse 488 (A21202, Invitrogen); anti-Rat 488 (A21208, Invitrogen); anti-Rabbit 488 (A21206,
882 Invitrogen); anti-Rabbit 546 (A10040, Invitrogen); anti-Goat 488 (A32814, Invitrogen); anti-
883 Goat 546 (A11056, Invitrogen); anti-Chicken 488 (SAB4600031, Sigma).

884 **In situ hybridization**

885 To detect SARS-CoV-2 RNA, in situ hybridization was performed on 12 μ m-thick sections of 4%
886 PFA-fixed OCT mounted on charged glass slides using the Leica Bond RX automated system
887 (Leica Biosystems, Richmond, IL). Heat-induced epitope retrieval (HIER) was conducted by

888 heating slides to 95°C for 15 minutes in EDTA-based ER2 buffer (Leica Biosystems, Richmond,
889 IL). Slides were treated in protease (Advanced Cell Diagnostics, Newark, CA) for 15 minutes
890 and probes hybridized to RNA for 1 minute. The SARS-CoV-2 probe (#848568, Advanced Cell
891 Diagnostics, Newark, CA) was detected using the Leica RNAScope 2.5 LS Assay-RED kit with
892 a hematoxylin counterstain (#322150, Leica Biosystems, Richmond, IL). An RNAPol2 probe
893 served as a host gene control to evaluate RNA quality; a probe for the bacterial *dap2* gene served
894 as a negative control ISH probe.

895 **Confocal Imaging and Quantification**

896 Immunostaining images were obtained using a Zeiss LSM 780 confocal microscope equipped
897 with a 40x, numerical aperture 1.1 water objective. The following laser lines were used DPSS
898 561nm (detection range 560-612nm) for Alexa Fluor 546; Diode 405nm (detection range 410-
899 480nm) for DAPI; and Argon 488nm (detection range 490-550nm) for Alexa Fluor 488. Images
900 for the same primary antibody across different samples were acquired and exported under the
901 same settings. Before exporting, contrast adjustment was applied as necessary for individual
902 channels using Zen lite (Zeiss) under the “Display” option. Images were cut by Photoshop and
903 assembled by Illustrator.

904 For quantification, at least 5 images were collected from each specimen using 40x objectives
905 under the tile scan and z stack mode at same depth. Positive cells were identified according to the
906 subcellular staining pattern and were counted manually using “Events” function of Zen lite
907 (Zeiss). Cells in olfactory or respiratory mucosa were quantified per mm of surface epithelium.
908 By measuring the whole length of Tuj1⁺ epithelium, The SARS-CoV2 infected axons were
909 quantified per μm diameter of axon bundle. Microglia in the olfactory bulb or shedding cells in
910 nasal cavity were quantified per mm^2 tissue.

911 **RNA isolation, cDNA synthesis and qPCR**

912 Total RNA was isolated from hamster olfactory tissue lysate using a Direct-zol RNA Kits
913 (Zymo). Equal amounts of RNA were transcribed into cDNA by High-Capacity cDNA Reverse
914 Transcription Kit (Applied Biosystems). On-Column DNase I digestion was conducted to
915 remove genomic DNA contamination. Ten nanograms of cDNA was added to a 20- μ L PCR
916 reaction using SYBR Green PCR Master Mix or TaqMan Fast Universal PCR Master Mix
917 (Applied Biosystems) on StepOne Plus System (Applied Biosystems). For SYBR Green PCR,
918 post-amplification melting curve analysis was performed to monitor unspecific products. Fold
919 change in mRNA expression was calculated using the comparative cycle method ($2^{-\Delta\Delta C_t}$). SYBR
920 Green PCR primer sequences of hamster genes are: ACE2: Forward,
921 TGGTGGGAGATGAAGCGAGA, and Reverse, GAACAGAGCTGCAGGGTCAC; OMP:
922 Forward, CAGAAGCTGCAGTTCGACCG, and Reverse, CAGAAGATTGCGGCAGGGTC;
923 Ifng: Forward, TAATGCACACCACACGTTGC, and Reverse,
924 AAGACGAGGTCCCCTCCATT. GAPDH: Forward, GTGGAGCCAAGAGGGTCATC, and
925 Reverse, GGTTACACCCATCACAAACAT. Mouse genes are: Nrp1: Forward,
926 CAGTGGCACAGGTGATGACT, and Reverse, ACCGTATGTCGGGAACTCTGAT; ACE2:
927 Forward, CCATTGGTCTTCTGCCATCCG, and Reverse, CCAACGATCTCCCGCTTCATC;
928 GAPDH: Forward, TCAATGAAGGGGTCGTTGAT, and Reverse,
929 CGTCCCGTAGACAAAATGGT.

930 **Single cell RNA-seq analysis**

931 Sc-RNA-seq dataset was retrieved from published study (GSE155006) by Mogilenko, et al⁴⁶.
932 This dataset was generated from sorted lung CD45⁺ immune cells from 3 or 17-month-old mice.
933 The Seurat R package was used for subsequent analysis. Quantity control was conducted

934 according to the standard pre-processing workflow. Cells in young and old datasets express 500-
935 2500 genes, mitochondrial genes less than 5% were selected and normalized using a scaling
936 factor 10,000. The highly variable genes in each dataset were selected using the
937 *FindVariableFeatures* function, and combined (10,228 cells in total) for Seurat integration
938 procedure and linear dimensionality reduction. The top 2000 most variable genes per dataset
939 were used for downstream principal component analysis and clustered using the *FindClusters*
940 function. The datasets include 16 clusters were then projected as UMAP plots. According to the
941 expression levels of canonical marker genes, we matched the clusters to known immune cell
942 types. We applied *FindMarkers* function to identify differentially expressed genes in
943 macrophages/dendritic cell lineage between young and old conditions. Average Log₂ fold
944 changes of gene expression and the percentage of cells expressing certain genes in each
945 condition were calculated.

946 **Statistical analyses**

947 Data are expressed as mean ± SD. as indicated. Data analyses were carried out using GraphPad
948 Prism. For experiments with two groups, *P* values were calculated using the unpaired two-tailed
949 Student's t-test. Differences were considered significant when $P < 0.05$.

950 **Reporting Summary.** Further information on research design is available in the

951 Nature Research Reporting Summary linked to this article.

952 **Data and materials availability:** Data, code, and materials will be made available upon request.

953 **Acknowledgements**

954 We are grateful to patients consenting to donate specimens for research. We thank Andrew
955 Johanson and Riley Richardson for RNAscope analysis. These studies were supported through
956 the generosity of the collective community of donors to the Johns Hopkins University School of

957 Medicine for COVID research. This work was funded by NIH Grants R01 AI132590, R01
958 DC016106 (A.P.L) and NIAID HHS N2772201400007C (AP).

959 **Author contributions:** M.C., A.P.L., and A.P. designed research; M.C. and W.S. performed
960 experiments; M.C. performed the bioinformatic analysis of the single cell RNA-seq dataset;
961 A.P., R.Z. performed *in vitro* infection experiments; N.R.R., A.P.L., M.R., H.K., and Z.L.
962 collected biopsies; J. V., S. B., and J. M. performed animal infection experiments; M.C., A.P., J.
963 M., K. W. and A.P.L. analyzed data; M.C., A.P., and A.P.L. wrote the paper.

964 **Competing interests:** The authors declare no competing interests.

Figure 1

Chen and Lane et al.

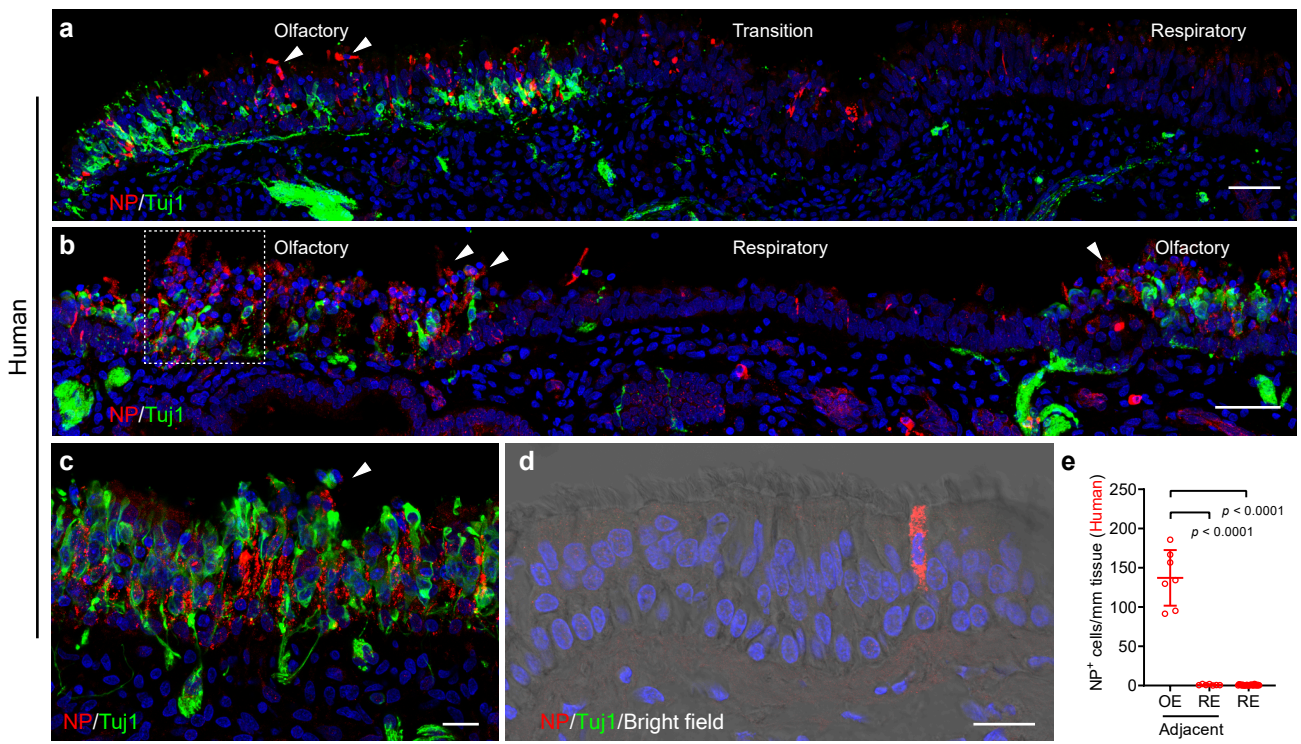


Figure 2

Chen and Lane et al.

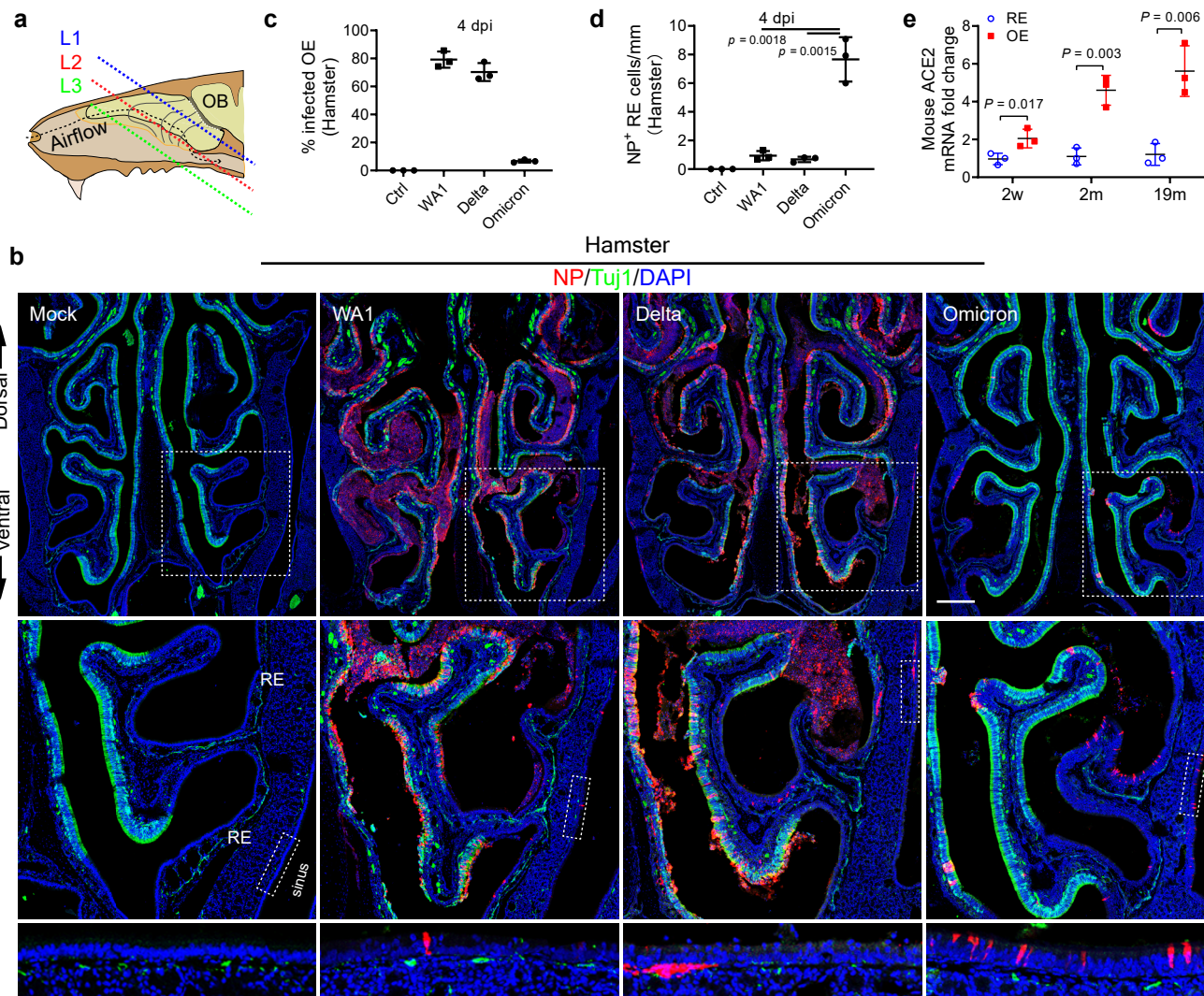


Figure 3

Chen and Lane et al.

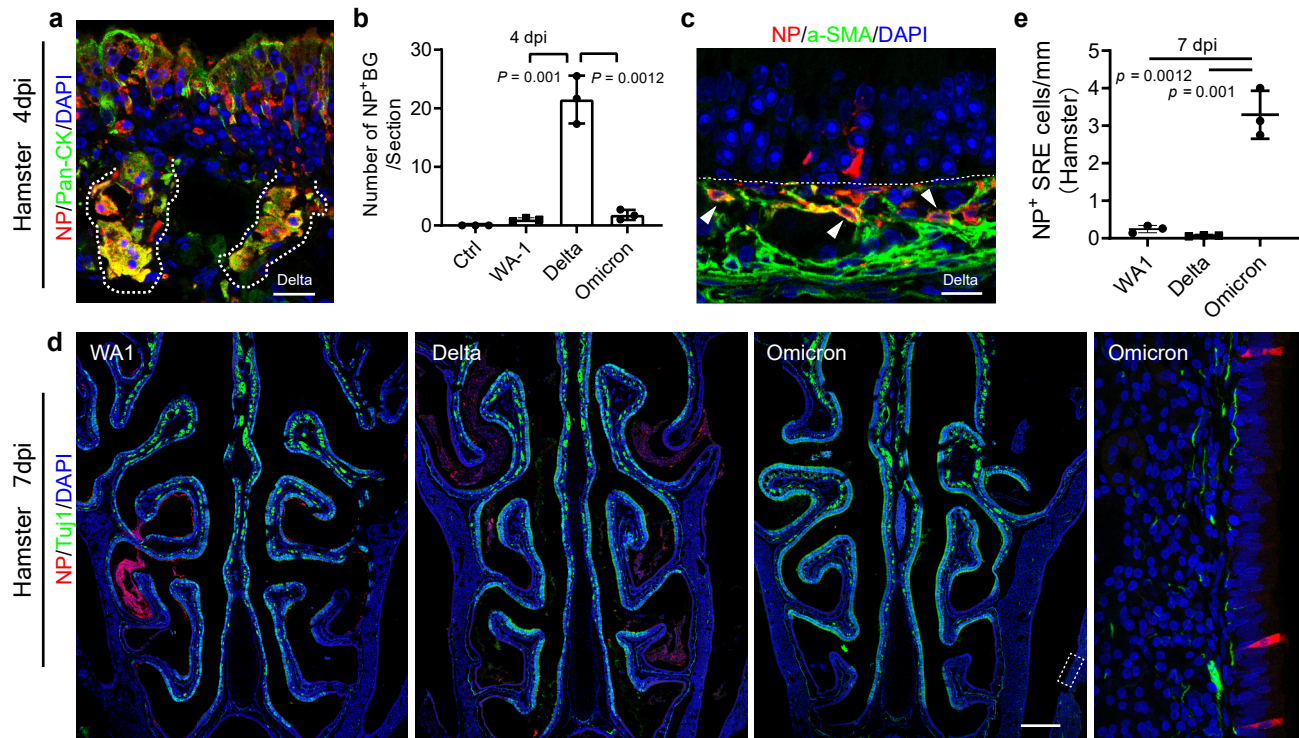


Figure 4

Chen and Lane et al.

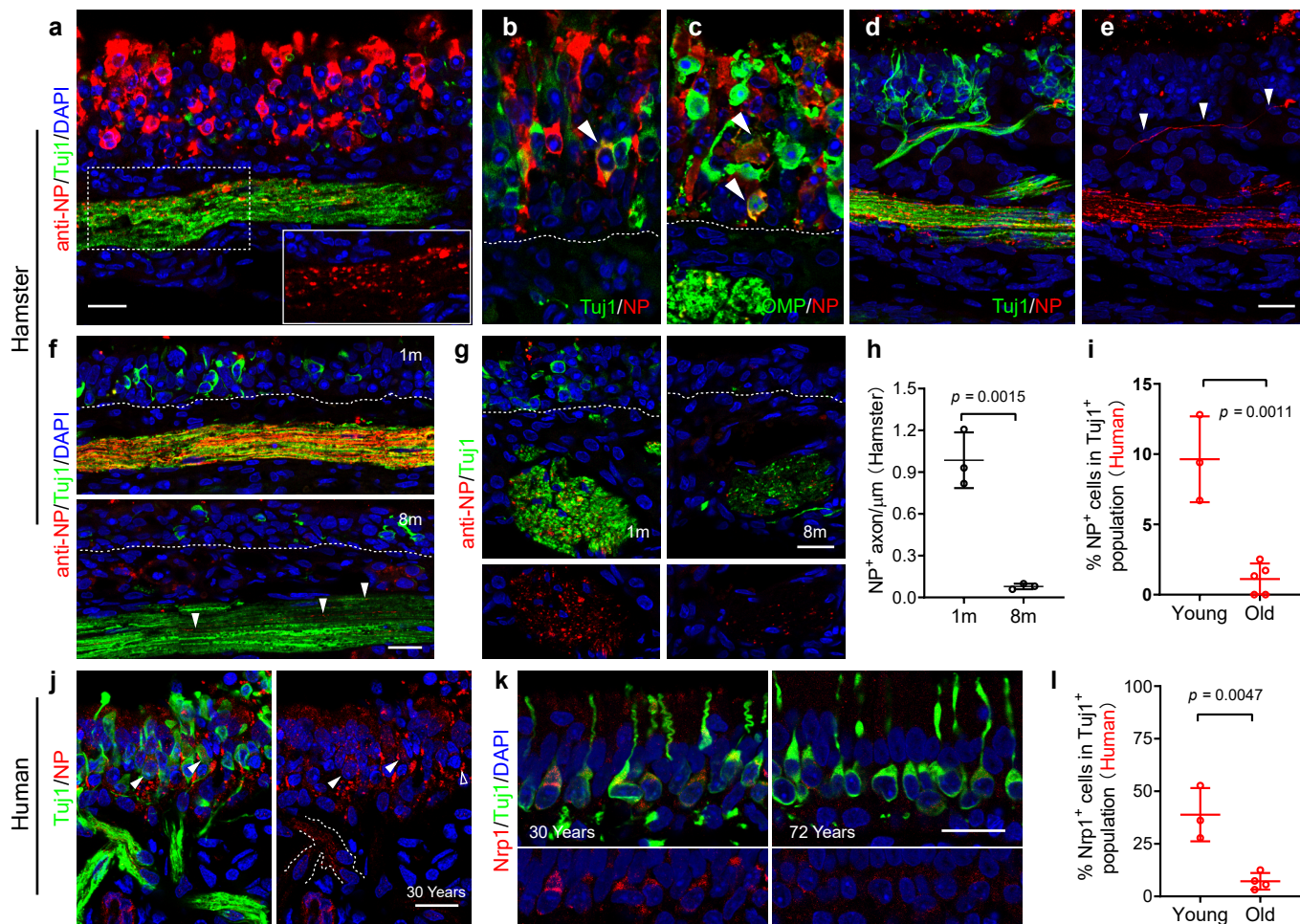


Figure 5

Chen and Lane et al.

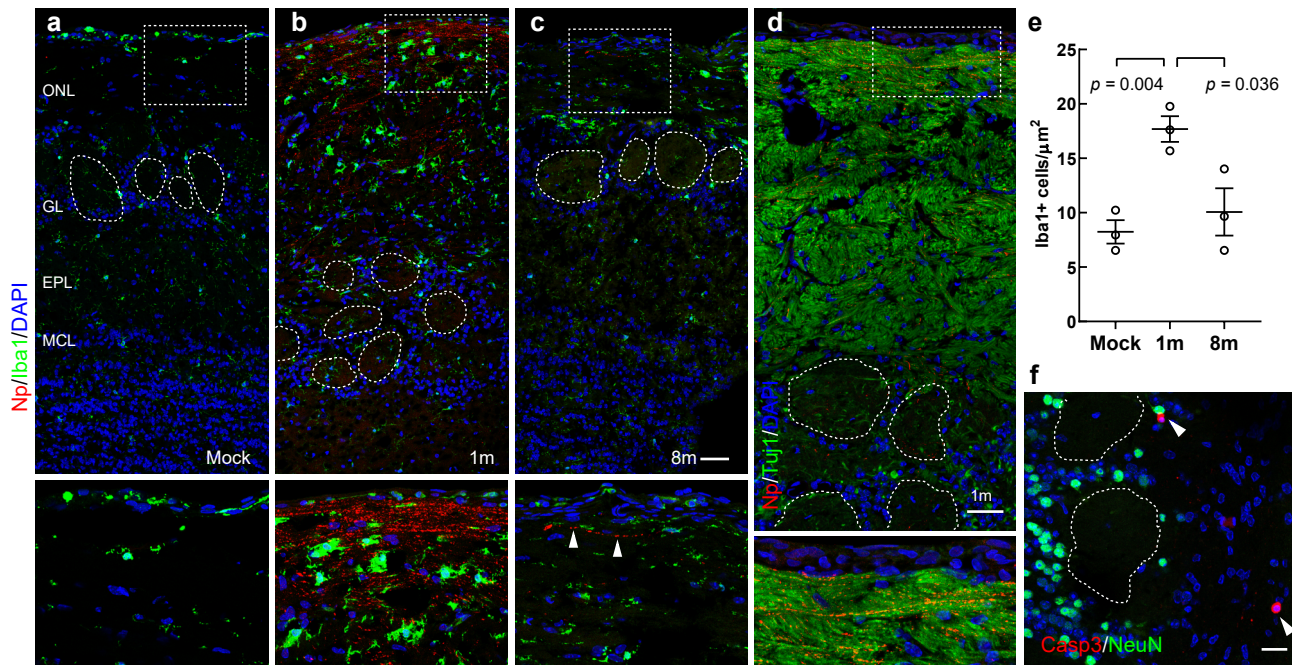


Fig 6

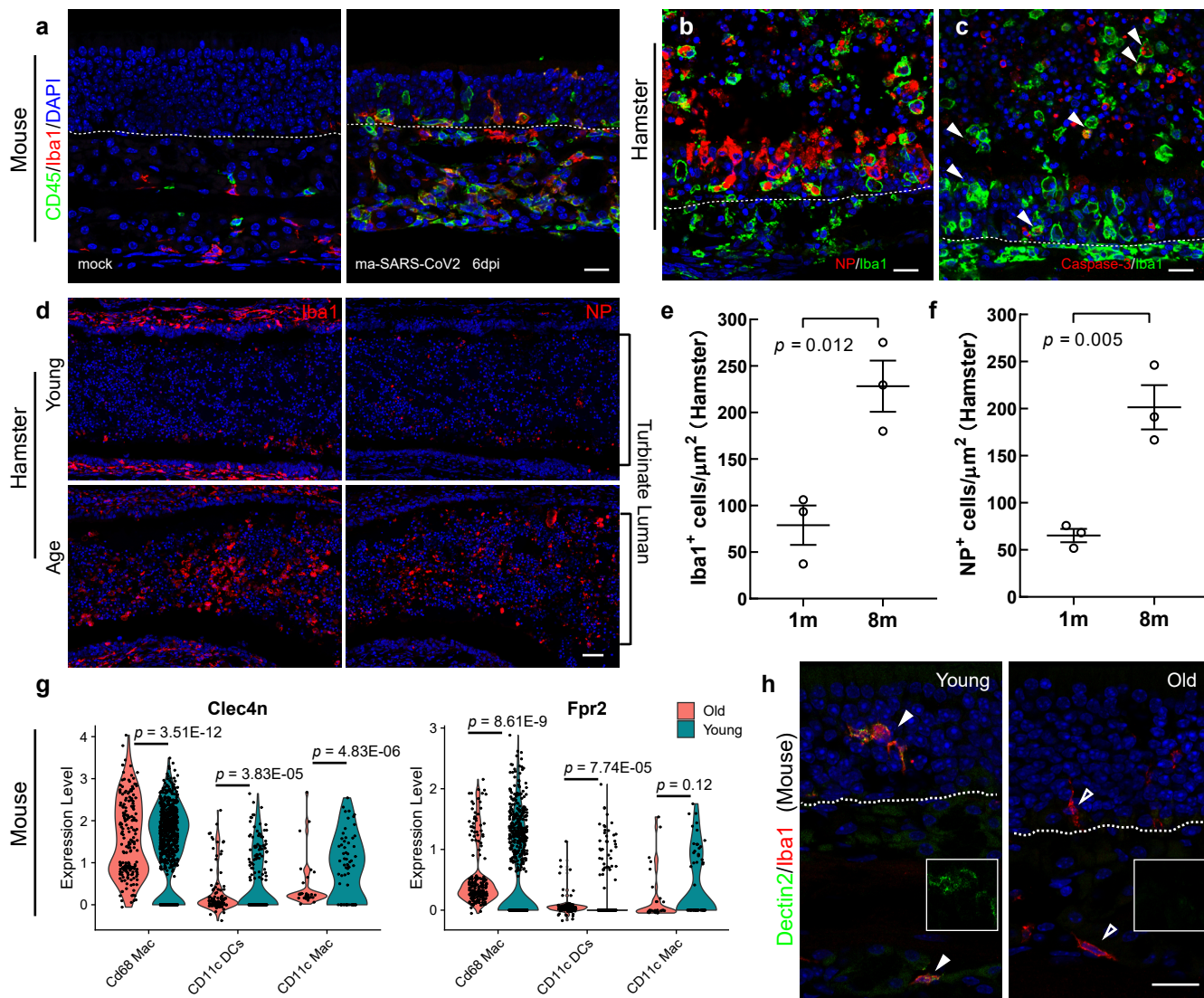
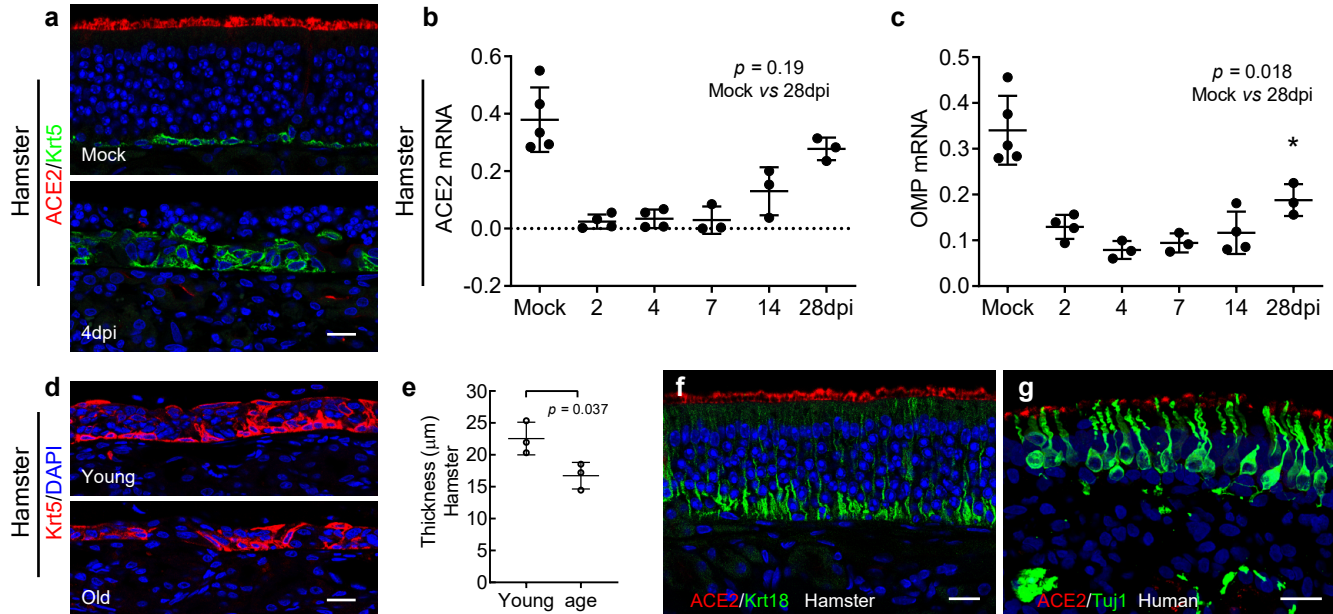
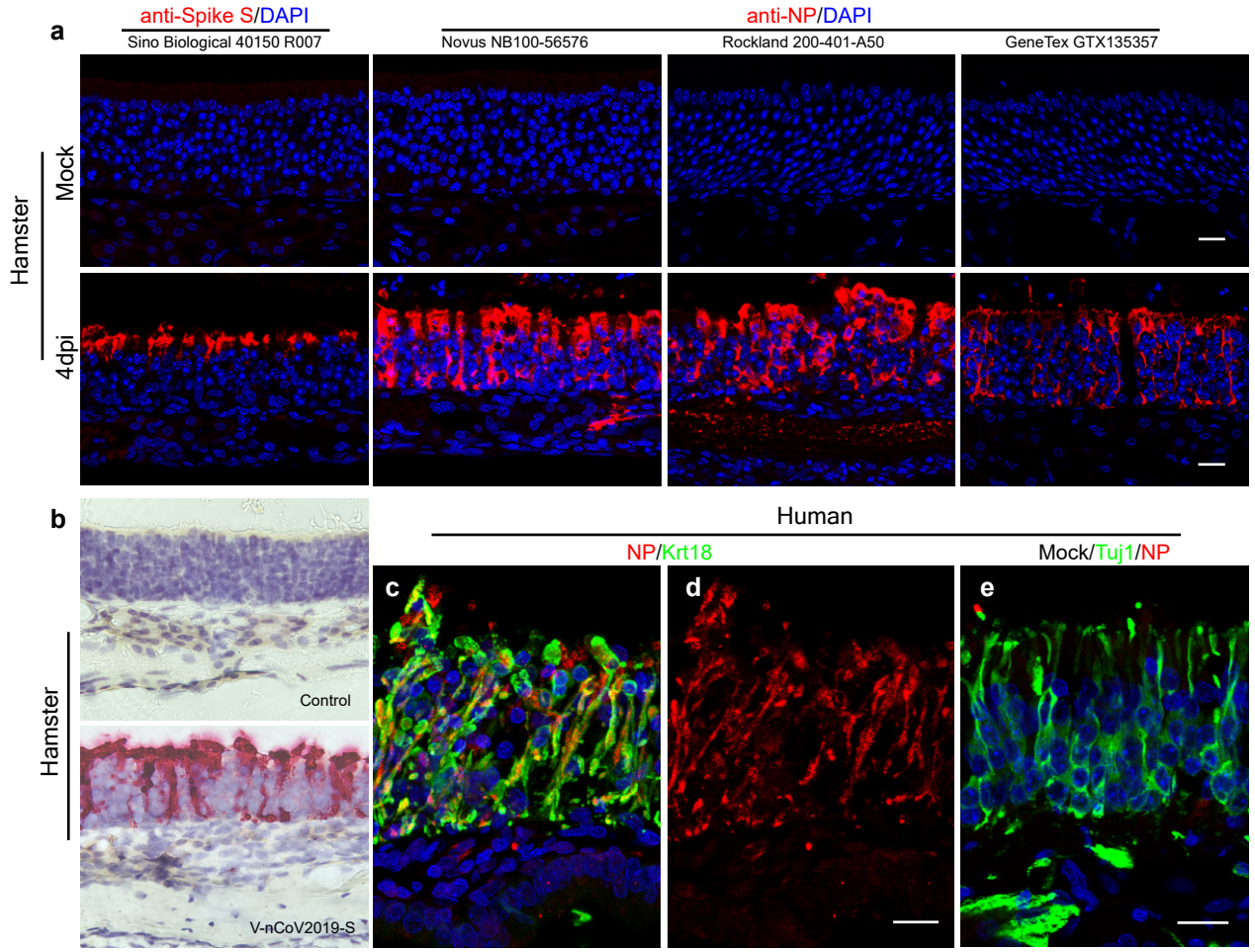
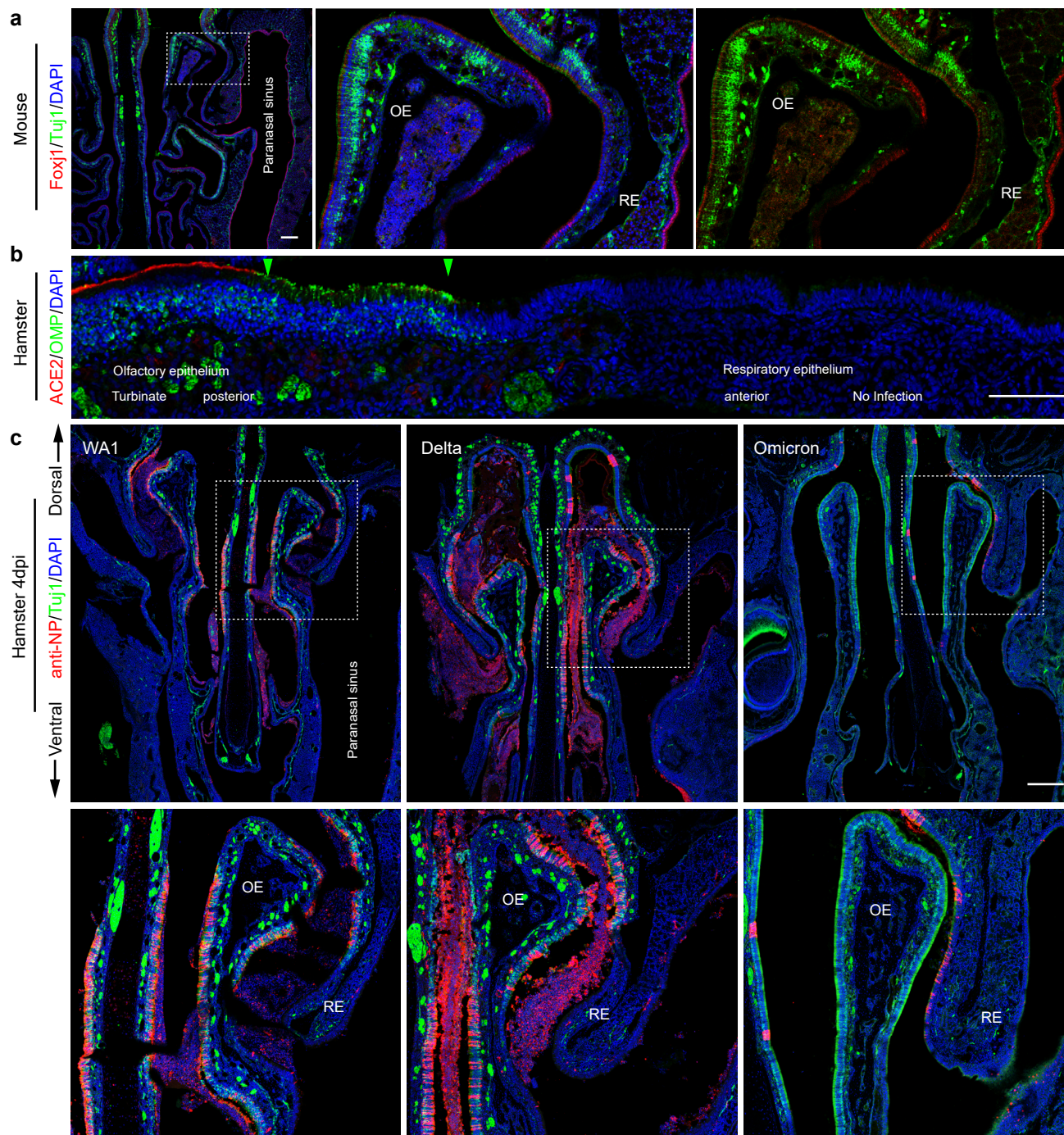


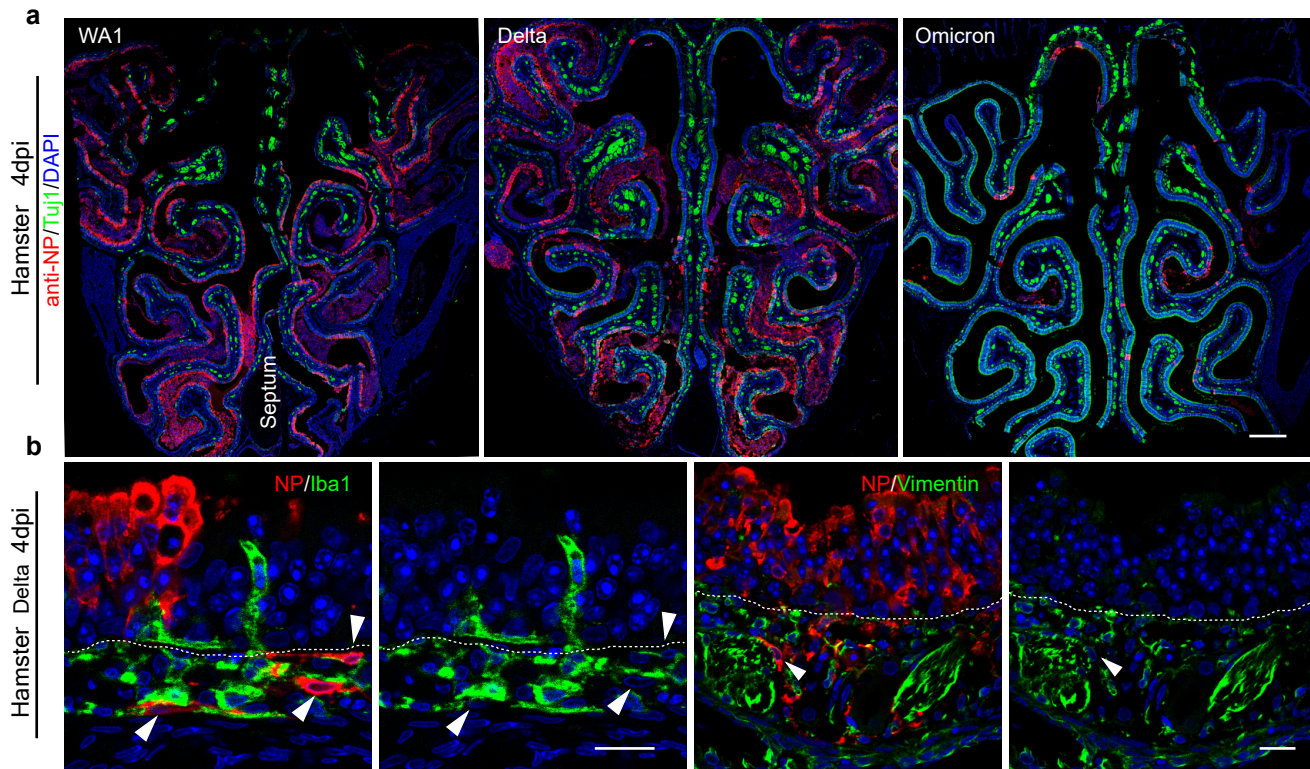
Figure 7

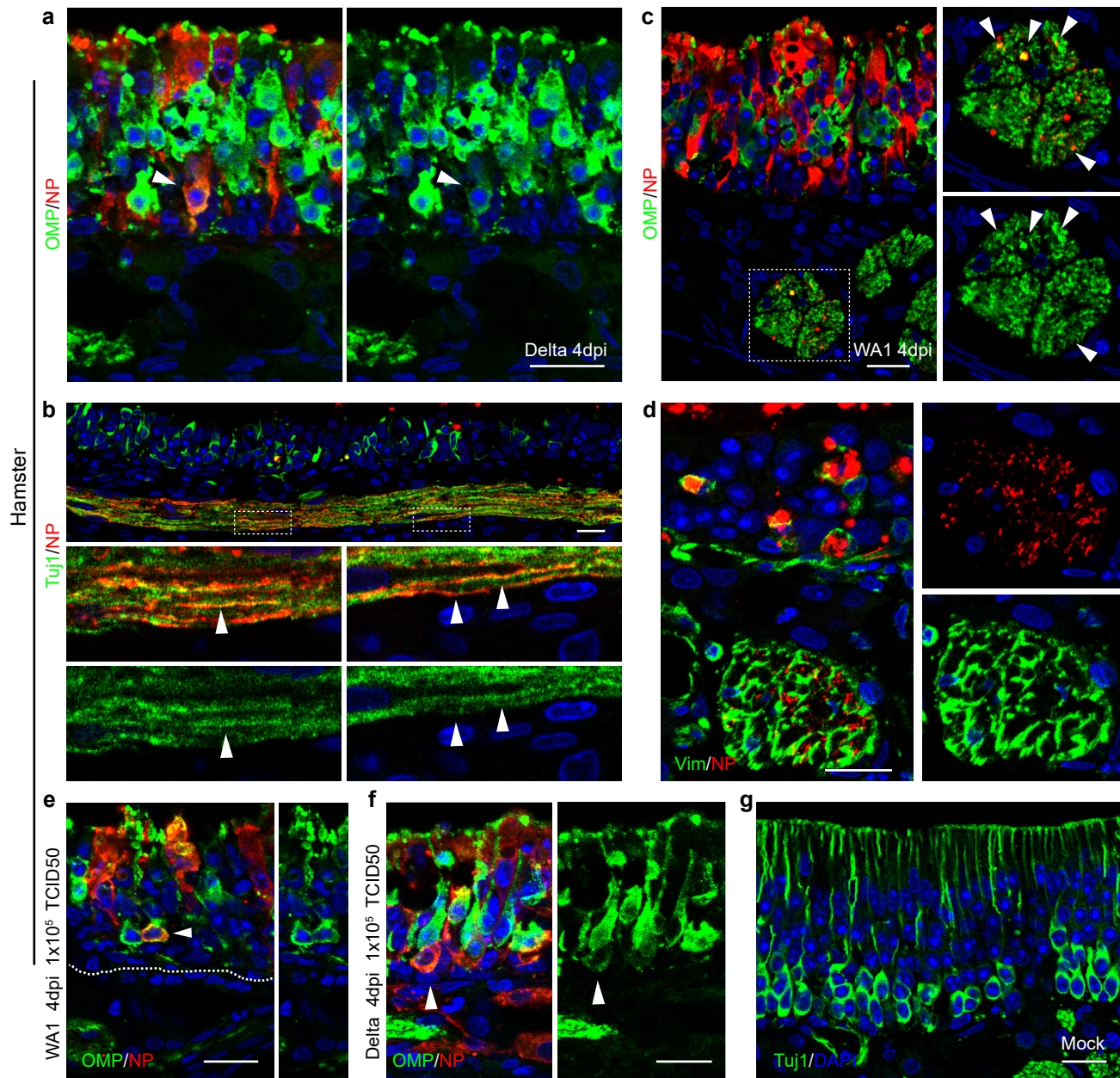
Chen and Lane et al.











Extended Data Fig. 5

Chen and Lane et al.

